

Numerical Simulations of Hot Halo Gas in Galaxy Mergers

Manodeep Sinha^{1*}, Kelly Holley-Bockelmann¹

¹ *Department of Physics & Astronomy, Vanderbilt University*

7 September 2018

ABSTRACT

Galaxy merger simulations have explored the behaviour of gas within the galactic disk, yet the dynamics of hot gas within the galaxy halo has been neglected. We report on the results of high-resolution hydrodynamic simulations of colliding galaxies with hot halo gas. We explore a range of mass ratios, gas fractions and orbital configurations to constrain the shocks and gas dynamics within the progenitor haloes. We find that : *(a)* A strong shock is produced in the galaxy haloes before the first passage, increasing the temperature of the gas by almost an order of magnitude to $T \sim 10^{6.3}$ K. *(b)* The X-ray luminosity of the shock is strongly dependent on the gas fraction; it is $\gtrsim 10^{39}$ erg/s for halo gas fractions larger than 10%. *(c)* The hot diffuse gas in the simulation produces X-ray luminosities as large as 10^{42} erg/s. This contributes to the total X-ray background in the Universe. *(d)* We find an analytic fit to the maximum X-ray luminosity of the shock as a function of merger parameters. This fit can be used in semi-analytic recipes of galaxy formation to estimate the total X-ray emission from shocks in merging galaxies. *(e)* ~ 10 -20% of the initial gas mass is unbound from the galaxies for equal-mass mergers, while 3 – 5% of the gas mass is released for the 3:1 and 10:1 mergers. This unbound gas ends up far from the galaxy and can be a feasible mechanism to enrich the IGM with metals.

Key words:

galaxies: formation - galaxies: evolution - galaxies: haloes - galaxies: interactions - intergalactic medium - methods:N-body simulations - X-rays: galaxies - hydrodynamics.

1 INTRODUCTION

Galaxy mergers drive galaxy evolution; they are one mechanism by which galaxies grow. The merger process is also accompanied by a strong gas inflow towards the central region (Barnes & Hernquist 1991; Mihos & Hernquist 1994; Combes et al. 1994; Hernquist & Mihos 1995; Sanders & Mirabel 1996) triggering a central starburst and perhaps an AGN. Consequently, galaxy mergers have been studied quite extensively both numerically (Holmberg 1941; Toomre & Toomre 1972; Barnes & Hernquist 1992, 1996; Mihos & Hernquist 1996; Springel & White 1999; Dubinski et al. 1999; Barnes 2002) and observationally (Schweizer 1986; Roberts et al. 2002; Laine et al. 2003; Casasola et al. 2004). However, none of these galaxy merger simulations included the hot gas in the galactic halo that is expected from standard galaxy formation theory (White & Rees 1978; White & Frenk 1991). In this paper, we explore the effect of hot halo gas during galaxy mergers with high-resolution numerical simulations.

Semi-analytic galaxy formation models have long predicted the existence of an extended reservoir of hot halo gas around spiral galaxies (White & Rees 1978; White & Frenk 1991). In this scenario, gas falling into the dark matter potential shock-heats to the virial temperature, $T_{\text{vir}} = 10^6 \text{K} (v_{\text{circ}}/167 \text{km/s})^2$ and subsequently cools over a characteristic time-scale, $t_c = kT/n_i\Lambda(T)$, that depends on the temperature T , the number density n_i and the cooling function $\Lambda(T)$. This gas cools via thermal bremsstrahlung and atomic line emission processes, with the majority of the radiation occurring in the soft X-ray band. The expected X-ray luminosity, L_X , is a steep function of the circular velocity, $v_{\text{circ}} - L_X \propto v_{\text{circ}}^5$. Since the effect of mass (circular velocity) on this halo X-ray luminosity is so non-linear, any attempts to observe the X-ray signature of this gas

* E-mail: manodeep.sinha@vanderbilt.edu, k.holley@vanderbilt.edu

would naturally be biased towards very massive haloes. Consequently, hot gas in massive elliptical galaxies has been shown by X-ray observations of cluster galaxies as well as in isolated ellipticals (see Mathews & Brighenti 2003, and references therein). Observations of massive ellipticals show that the X-ray luminosity is non-stellar in nature (O’Sullivan et al. 2001) leading credence to its hot gaseous origin. An extended gaseous halo in a quiescent spiral has been observed *only* for the massive spiral NGC 5746 (Pedersen et al. 2006).¹ However, the existence of a hot, rarefied and extended galactic halo has been inferred from OVI absorption lines in high velocity clouds in the vicinity of the Milky Way (Sembach et al. 2003). The density of this halo gas ($n_{\text{H}} \sim 8 \times 10^{-5} \text{cm}^{-3}$) (Murali 2000; Snowden et al. 1997) is consistent with the predicted density for a Milky Way type galaxy. Given the existence of hot halo gas, it is important to include it in galaxy merger simulations.

During a merger, the bulk motion of the galaxy gas is converted into thermal energy via shocks. The orbital velocity of the gas during a merger is ≥ 100 km/s whereas the sound speed is ~ 10 km/s. This can produce strong shocks with Mach numbers > 10 . Assuming an adiabatic index of 5/3, the shocks may heat the gas to:

$$T_{\text{final}} = \frac{3 \mu m_{\text{H}}}{16k} v_{\text{initial}}^2, \quad (1)$$

where T_{final} is the gas temperature after the shock, μ is the mean molecular weight, m_{H} is the proton mass, k is the Boltzmann constant, and v_{initial} is approximately equal to the radial velocity prior to the collision. Nearly 50% of the kinetic energy can be converted into thermal energy of the gas particles. Thus, we expect that the hot gas will shock-heat and radiate in soft X-rays. The shocks may occur as soon as the gaseous haloes collide – well before the optical extents of the galaxies begin to show signs of morphological disturbance.

This hot halo gas may play an important role in enriching the intergalactic medium (IGM). Galaxy formation theory predicts that baryons fall into the dark matter potential and shock-heat. Absorption lines reveal the presence of diffuse gas with column density $N_{\text{H}} \gtrsim 10^{14} / \text{cm}^2$ (Fransson & Epstein 1982; Cowie et al. 1995; Wang 1995). At $z \sim 3$, most of the baryonic mass is in the Lyman- α forest (Fukugita, Hogan, & Peebles 1998). The baryon fraction in the Lyman- α forest systematically decreases with z and is almost zero at present. It would be reasonable to expect that all the baryons are now part of galaxies in the form of stars and the interstellar medium. However, recent estimates of the mass fraction of baryons in different components still fail to detect $\sim 60\%$ of the total baryon content at low z , with 6% in stars in galaxies (Fukugita & Peebles 2004), 2% in neutral gas (Zwaan et al. 2003), 4% in galaxy clusters and galaxy groups (Allen et al. 2002) and $29 \pm 4\%$ in low- z Lyman- α absorbers (Penton et al. 2004; Danforth & Shull 2008). The consensus is that the majority of the ‘missing’ gas is located in regions of low over-density, $\delta\rho/\rho \sim 10^0 - 10^2$ with temperatures in the range $10^5 - 10^7$ K. This is the Warm-Hot Intergalactic Medium (WHIM) and is currently one of the most elusive astrophysical objects (for a recent review see Bregman 2007). Numerical simulations predict that the WHIM must reside in filaments and relatively low over-density regions (Cen & Ostriker 1999; Davé et al. 1999; Cen & Ostriker 2006; Davé & Oppenheimer 2007). Numerous efforts have been taken to detect and characterise the WHIM; however, most of the observations to date are not iron-clad and have required some fine-tuning in the fitting procedure for the data to come up with a significant detection (Nicastro et al. 2005; Mathur et al. 2003). The current instrumentation limits on the *Chandra* and *XMM-Newton* are a major hold-up in the discovery of the WHIM; next generation X-ray telescopes like *Constellation-X* should be capable of detecting the absorption lines from the WHIM along the line of sight to bright background sources.

The immediate question is: How does gas get into the WHIM state? Some form of mass and energy injection is essential to create this hot reservoir of gas, and this form of feedback must also account for the metals in the IGM. Numerical simulations of structure formation must incorporate various baryonic processes such as supernova feedback (Mac Low & Ferrara 1999; Borgani et al. 2002; Thacker & Couchman 2000; Scannapieco et al. 2006; Governato et al. 2007), starburst-driven galactic winds (Springel & Hernquist 2003; Oppenheimer & Davé 2008) and AGN feedback (Springel et al. 2005; Di Matteo et al. 2005; Scannapieco et al. 2005; Thacker et al. 2006; Hopkins et al. 2006; Croton et al. 2006; Sijacki et al. 2007; Bhattacharya et al. 2008; Di Matteo et al. 2008). All these energy delivery mechanisms are more effective in low mass galaxies (Scannapieco et al. 2008), e.g., these prescriptions blow-out the gas in dwarf galaxies (Mac Low & Ferrara 1999; Kobayashi et al. 2007). *However, this is in direct disagreement with observational results that show dwarf galaxies to be more gas-rich* (Kannappan 2004). In this paper, we will explore if galaxy mergers, which are ubiquitous, can be used to fuel the IGM.

Observations of major galaxy mergers show that the merger rate evolves rapidly, increasing from $\sim 5\text{-}10\%$ at $z \sim 1$ to $\sim 50\%$ at $z \sim 3$ (Conselice et al. 2003). Integrating this merger rate suggests that a typical massive galaxy will undergo 4-5 major mergers between $z \sim 3$ and $z \sim 0$, with most of these mergers occurring at $z > 1.5$. Numerical simulations can be used to explore the evolution of the merger rate as well as the merger ratio with z . Fakhouri & Ma (2008) analyse the *Millennium Simulation* to constrain this evolution and find that a major merger (merger ratio $\geq 1/3$) occurs at the rate of 0.5 per halo per unit redshift. Minor mergers with $\xi \geq 1/10$ are far more common at all redshifts.

In this paper, we explore typical mergers with a Milky Way type primary galaxy. We sample the major mergers by

¹ It has since been shown that the detection of hot gas in NGC 5746 may be caused by contamination from unresolved point sources (J. Rasmussen, private communication).

simulating an equal-mass merger between two such galaxies. We also attempt to get the boundary of the major mergers for a merger ratio, $\xi \sim 1/3$ for our second set of merger ratios. Minor mergers are the most frequently occurring mergers in the Universe; we model this by simulating a merger with $\xi \sim 1/10$. This describes the three independent sets of simulations that we will perform to constrain the effect of the merger ratio on the behaviour of the hot gas during galaxy mergers. Mergers need an additional specification – the merger orbit. We will describe the parameters for specifying the content of the galaxies (see Sections 2.1 and 2.2), and construction of the merger orbits in Section 2.4. In Section 4 we will present the results of our numerical simulations of galaxy mergers. We will also derive an analytic fit for the peak shock X-ray luminosity and the unbound gas mass as a function of the progenitor galaxy masses and impact parameters. In Section 5 we discuss the implications of our results and future work.

2 METHOD

We create an equilibrium model for an isolated galaxy by numerically sampling for the joint distribution function (hereafter, DF) of the dark matter and gas. The DF for a spherically symmetric potential-density pair can be written as:

$$f(\mathcal{E}) = \frac{1}{\sqrt{8\pi^2}} \left[\int_0^{\mathcal{E}} \frac{d^2\rho}{d\Psi^2} \frac{d\Psi}{\sqrt{\mathcal{E} - \Psi}} + \frac{1}{\sqrt{\mathcal{E}}} \left(\frac{d\rho}{d\Psi} \right)_{\Psi=0} \right] \quad (2)$$

where, \mathcal{E} and Ψ are the absolute value of the total energy and the gravitational potential respectively and ρ is the density. We will describe the initialisation of the dark matter and the gas component in the following subsections.

2.1 Constructing a dark matter halo

Large scale cosmological simulations lead to a two-parameter universal dark matter halo density profile as shown by Navarro, Frenk, & White (1997) (hereafter, NFW). The key characteristics are the virial radius, R_{vir} such that the average density of the halo within that radius is a certain multiple ($\Delta_{200} = 200$) of the critical density of the universe, $\rho_{\text{crit}} = 3H_0^2/8\pi G$, and the concentration parameter, $c = R_{\text{vir}}/r_s$, where r_s is the scale radius of the NFW profile. Since the mass of the NFW halo is infinite, we implement an ad-hoc truncation radius for the dark matter (and the gas) at $R_{\text{halo}} = 1.2 \times R_{\text{vir}}$.

To compute the DF, we first create a logarithmically spaced array in r with 10^5 bins. The minima and maxima of the bins are fixed at 10^{-5} and 100 times the virial radius. Thus, we capture the inner cusp of the NFW halo profiles as well as the outlying particles with highly eccentric orbits; this can be seen from the upturn in the DF values for small E in Fig. 1. Note that the inner limit is much smaller than our softening length while the outer limit is much larger than the truncation radius of 1.2. This was done to ensure a higher accuracy of the DF itself, even though at present we can not reach such numerical resolution. On this finely-spaced grid, we define the values for $\rho(r)$, $M(r)$ and $\Phi(r)$ and obtain the derivatives by finite differencing. The DF is then obtained by numerically integrating Eqn. 2 with a using a fourth-order Runge-Kutta integrator. Following Lokas & Mamon (2001), we chose our system of units as $G = 1.0$, $M_{\text{vir}} = 1.0$, $R_{\text{vir}} = 2.0$ with the resulting $f(\mathcal{E})$ in units of $\sqrt{8}M_{\text{vir}}/(R_{\text{vir}}V_{\text{vir}})^3$.

Our fiducial galaxy is a Milky-Way type galaxy with a circular velocity of 160 km/s and a concentration parameter $c = 10$. M_{vir} for this primary galaxy is $1.36 \times 10^{12} M_{\odot}$ with $R_{\text{vir}} = 228.6$ kpc. The secondary galaxies for our merger simulations are chosen to be one-third and one-tenth of the mass of the primary; this translates approximately to circular velocities of 110 and 74 km/s. To determine the concentrations of such haloes, we use the analytic fitting formula of Bullock et al. (2001). With this prescription, our fiducial galaxy has a concentration of $c = 10$, and the concentrations for the two secondary galaxies are 16 and 25 respectively.

Fig. 1 shows the comparison between the DF from Lokas & Mamon (2001) for an NFW halo with $c = 10$ and the one obtained with our code for the fiducial galaxy with a 10% gas fraction.

2.2 Constructing a gas-rich galaxy halo

Now that the dark matter has been initialised, we need to initialise the gas. Earlier papers have used $\Omega_b/\Omega_{\text{dm}} \rho_{\text{dm}}$ as the ad-hoc density for the gas for cosmological simulations of structure formation. While that approximation is valid for *initial conditions* in a cosmological framework where the force field is completely determined by the dark matter (and gas merely falls into the dark matter potential), our simulations are in a fixed space-time and we needed an analytic physically motivated gas density profile. We chose the observationally verified β -profile (Cavaliere & Fusco-Femiano 1976; Jones & Forman 1984; Eke et al. 1998) used to model gas in galaxy clusters, a more massive analog to our gaseous haloes. The gas is isothermal and in hydrostatic equilibrium. We use $\beta = 2/3$ and a core of $r_c = r_s/3$, giving a density profile:

$$\rho_{\text{gas}} = \frac{\rho_0}{1 + (r/r_c)^2}. \quad (3)$$

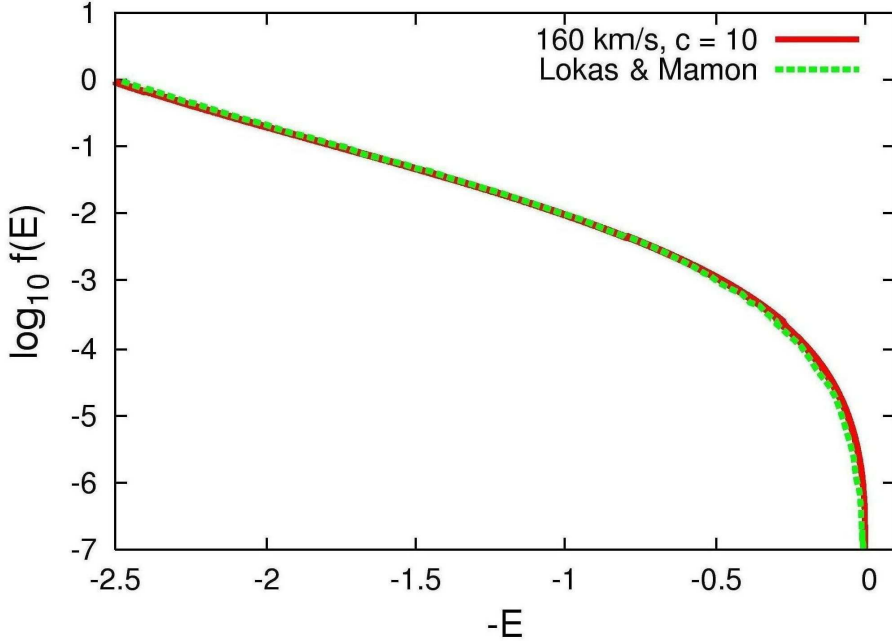


Figure 1. The computed DF for our fiducial galaxy with $c = 10$ and 10% gas fraction. Overplotted in magenta is the DF from Lokas & Mamon (2001) for a dark matter only NFW halo with $V_{\text{vir}} = 160$ km/s and $c = 10$. The presence of the gas makes very little difference in the overall DF.

Since the density profile is spherically symmetric, we employ the Eddington inversion method to compute the DF for the joint dark matter and gas distribution. For the dark matter component, position-velocity pairs are drawn from this DF. For the gas, we chose the position from the gas density. However, the gas velocity depends on the temperature and the temperature itself can not be freely assigned since it is determined by the overall gas density-potential pair. We assume that the gas is polytropic and follows an equation of state, $P \propto \rho^{5/3}$ where P and ρ are the pressure and density of the gas. Finally, we assume hydrostatic equilibrium to compute the temperature of the gas self-consistently. The gas is assumed to be at virial temperature at the virial radius with a central density constrained by the total amount of gas in the halo. Once the temperature has been assigned to the gas particles, we calculate the velocity dispersion by assuming virialization. The final gas velocities are drawn from a Gaussian distribution with zero mean velocity and a velocity dispersion given by $\sigma^2 = 2kT/(\gamma - 1)\mu m_H$.

The input parameters to our galaxy initialisation code are the circular velocity of the halo, the number of halo particles, the gas fraction and the number of gas particles. Our fiducial galaxy is similar to the Milky Way with $V_{\text{vir}} = 160$ km/s. To investigate the role of mass-ratio during mergers, we constructed galaxies with 1/3 and 1/10 of the mass of our fiducial galaxy. For a galaxy with one-third the mass, the virial velocity is 110 km/s and for one-tenth the mass, the virial velocity is 74 km/s. Since we aim to simulate the mergers of two different mass galaxies, it was imperative to have the same mass per particle between each of the galaxies to prevent spurious numerical relaxation. Thus, the number of particles in the secondary galaxies are set by the corresponding number in the primary galaxy. We use a fixed number of 5×10^5 particles for dark matter and gas in the primary galaxy for all the gas fractions. Since the total halo mass of the primary galaxy is fixed, our halo mass resolution is $3 \times 10^6 M_{\odot}$, independent of the gas fraction. The gas mass resolution for the 1%, 10% and 18% gas fractions in the primary galaxy is 1.5×10^6 , 1.5×10^7 and $2.7 \times 10^7 M_{\odot}$ respectively (see Table 1).²

Since we are exploring how gas-rich galaxies behave during galaxy mergers, we did not want the input temperature profile, $T(r)$, to vary and devised a multi-step process to reduce this temperature evolution. Initially, the gas temperature is determined from the hydrostatic equilibrium condition in the joint dark matter and gas potential. Then the gas velocity is assigned from the velocity dispersion based on virial equilibrium. The problem is that this assumption is not valid in the inner regions of the galaxy; even in isolation, the central gas particles shock-heat, increase their temperatures and decrease their velocity dispersion rapidly. A higher artificial viscosity parameter (AVP) aids this transformation and the core temperatures can increase by as much as a factor of 2 from the originally solved temperature profile. To alleviate this problem, after initialising the galaxy with the method described above, we instead evolve the galaxy model in isolation with AVP of 0.5 to allow the gas particles to attain a new equilibrium temperature profile (see next section on the choice of AVP). This is

² Note that this gas mass resolution is the product total number of neighbours of a gas particle, 50, and the mass of each gas particle.

the first iteration on an equilibrium temperature profile for the halo gas. We find that the new temperature profile is indeed larger at the centre and turns over at the outer edge with an exponential drop-off near $r \gtrsim 0.5 R_{\text{vir}}$. We fit this temperature profile and apply it as a second iteration on the initial temperature profile for our model (see Fig. 2 for a comparison of the two iterations). This evolved temperature profile is nearly flat to $\sim 0.5 R_{\text{vir}}$ and is consistent with observations of galaxy clusters showing that the temperature stays to within 40% of the central temperature out to $0.6 R_{\text{vir}}$ (Leccardi & Molendi 2008; Vikhlinin et al. 2005).³ Finally, we evolve the galaxy with zero artificial viscosity over a period of ~ 1 Gyr to get rid of dynamical irregularities in our temperature profile fit (see Fig. 3). Since there is absolutely no entropy increase with zero artificial viscosity, our temperature profile essentially remains constant in this step. We re-calculate M_{vir} , R_{vir} and L_X (see Table 2) after iterating the initial conditions. For the primary galaxy, the maximum change in R_{vir} is $\sim 2.5\%$; for the one-third galaxy and the one-tenth galaxy, the corresponding changes are $\sim 3\%$ and $\sim 2.6\%$ respectively. Once the galaxies are initialised, we check for stability by evolving them in isolation. One of the key ways of ascertaining the equilibrium of multi-component systems is by computing the *Virial of Clausius*, VC . An equilibrium model for a galaxy should have VC fairly close to 1. The numerical models for our galaxies in the first iteration have a $VC \sim 1.2$, irrespective of the gas fraction or the halo size. Thus, while being close to equilibrium, the galaxies are not exactly in steady state initially. The value of VC for the isolated galaxies with the iteratively-obtained temperature profile, ranges from 1.12 for the primary to ~ 1.07 for both the secondary galaxies.

To test the stability of this new galaxy model after iterating the temperature profile, we simulate this evolved galaxy with $\text{AVP} = 0.5$ for a Hubble time. We find that the change in the overall temperature profile drops to $\sim 10 - 20\%$ over this entire timespan. Our choice of softening length was guided by the suggested optimal softening from Power et al. (2003) with $\epsilon_{\text{opt}} \gtrsim 4 R_{\text{vir}} / \sqrt{N_{\text{vir}}}$ where N_{vir} is the number of particles within the virial radius. Our $\epsilon = 1.1$ kpc is comparable to the optimal value of $\epsilon_{\text{opt}} \approx 0.9$ kpc.

We use the parallel, hydrodynamic code GADGET-2 (Springel et al. 2001; Springel 2005) for all the numerical simulations in this paper. GADGET-2 computes the gravitational forces with a hierarchical tree algorithm (Barnes & Hut 1986) while gas particles receive additional hydrodynamic acceleration as calculated using Smooth Particle Hydrodynamics (Gingold & Monaghan 1977, hereafter SPH). The code explicitly conserves energy and entropy for the SPH particles and uses adaptive time-steps for the time-evolution. Since this is a first attempt to model the gas behaviour during the merger, cooling, star formation and radiative feedback have all been neglected.

³ Since the surface brightness decreases rapidly with radius, the signal in the outer regions is dominated by low photon counts and high background; consequently, the measurements are not as robust in the outskirts of clusters.

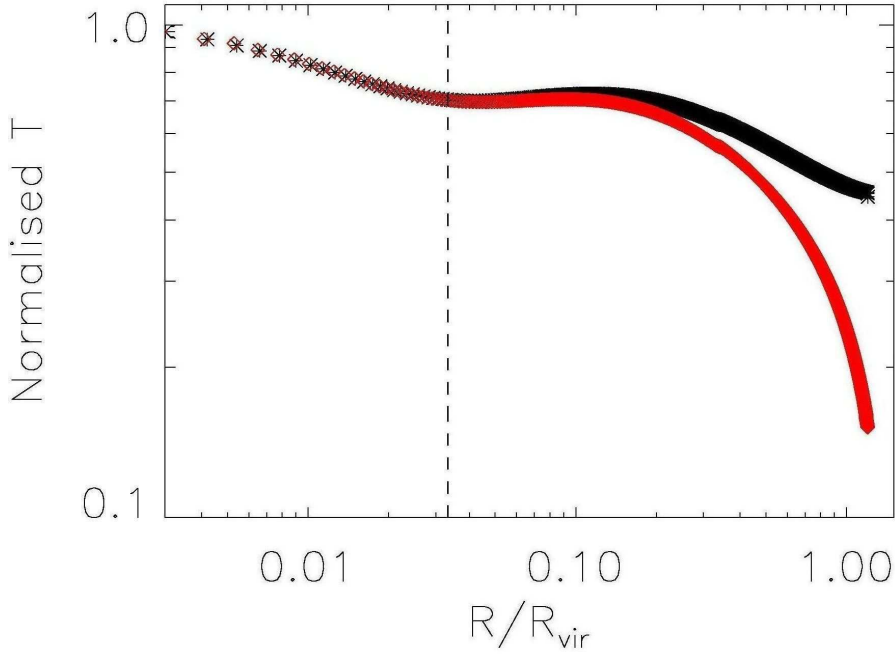


Figure 2. Creating a stable temperature profile. The black shows the spherically averaged temperature profile obtained for the gas in hydrostatic equilibrium. The red shows the temperature profile after an exponential drop-off has been added to the outer region. The dashed line shows the core radius, $r_c = R_{\text{vir}}/3c$ for the gas and corresponds to the location of the dip. The temperature drops from $0.7 T_{\text{vir}}$ at $0.2 R_{\text{vir}}$ to $0.4 T_{\text{vir}}$ at $0.6 R_{\text{vir}}$ and is consistent with observations of galaxy clusters (Vikhlinin et al. 2005; Leccardi & Molendi 2008).

Table 1: This table lists the parameters used to make the 9 isolated galaxy models. A constant physical softening of 1.14 kpc was used for both the gas and dark matter particles in all simulations. The number of particles used to model the two smaller galaxies was chosen such that the mass of each particle (dark matter and gas) was the same as the mass of the corresponding particle for the primary galaxy.

Gas Content	Galaxy Type	Conc.	v_{circ}	R_{vir}	M_{vir}	M_{DM}	N_{DM}^{\dagger}	Gas Mass Res. [§]
–	–	–	[km/s]	[kpc]	[$10^{10} M_{\odot}$]	[$10^{10} M_{\odot}$]	[10^5]	[$10^6 M_{\odot}$]
1% gas	Primary	10.0	160.0	228.6	136.1	150.0	5.0	1.5
	Onethird	16.0	110.0	158.5	45.3	48.0	1.6	1.5
	Onetenth	25.0	74.0	106.1	13.6	14.5	0.48	1.5
10% gas	Primary	10.0	160.0	228.6	136.1	150.0	5.0	15.0
	Onethird	16.0	110.0	158.5	45.3	48.0	1.6	15.0
	Onetenth	25.0	74.0	106.1	13.6	14.5	0.48	15.0
18% gas	Primary	10.0	160.0	228.6	136.1	150.0	5.0	27.0
	Onethird	16.0	110.0	158.5	45.3	48.0	1.6	27.0
	Onetenth	25.0	74.0	106.1	13.6	14.5	0.48	27.0

[†] The number of gas particles is the same as the number of halo particles in each galaxy.

[§] We used a fixed 50 SPH neighbours for all the simulations.

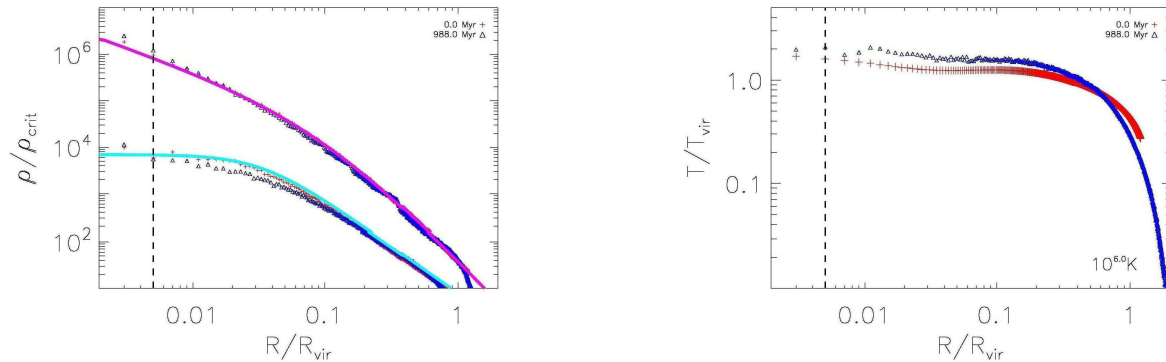


Figure 3. Evolution of gas density and temperature for a 10% gas fraction in our fiducial galaxy during initial condition construction. *Left:* The evolution for both the gas and dark matter is minimal; however, we see some outflowing features in the dark matter density. This results in a slightly larger galaxy at the end of 1 Gyr. The analytical input profiles shown in magenta (for dark matter) and cyan (for gas). The vertical dashed line is the softening used in the simulation. *Right:* The virial temperature is noted in the bottom-right. As the system evolves, the temperature profile drops off exponentially at roughly R_{vir} with a ‘knee’ around $\sim 0.5 R_{\text{vir}}$.

Table 2: This table lists some of the physical quantities for the galaxies after they were evolved with zero artificial viscosity for 1 Gyr. The mergers are generated from two galaxies in this table.

Gas Content	Galaxy Type	Unbound gas	L_X	R_{vir}	M_{vir}	Hot gas	Virial of Clausius
–	–	[%]	$[10^{40} \text{ erg/s}]$	[kpc]	$[10^{10} M_{\odot}]$	[%]	–
1% gas	Primary	0.36	0.10	224.3	128.9	70.0	1.11
	Onethird	0.50	0.03	154.5	42.1	46.0	1.08
	Onetenth	0.58	0.01	103.9	12.8	21.0	1.07
10% gas	Primary	0.62	8.87	223.4	126.5	79.0	1.12
	Onethird	0.43	3.17	153.9	41.6	48.0	1.08
	Onetenth	0.56	0.88	103.7	12.8	24.0	1.06
18% gas	Primary	0.68	26.5	222.9	126.3	77.0	1.12
	Onethird	0.42	10.9	153.6	41.3	50.0	1.08
	Onetenth	0.50	2.75	103.3	12.6	25.0	1.06

2.3 Dependence on Artificial Viscosity

Since the AVP determines the strength of the shocks produced in the simulation, we test the effect varying the AVP. We evolve the primary galaxy with a 10% gas fraction in isolation, with varying AVP from 10^{-4} – 1.0. Note that the recommended range of AVP is 0.1 – 1.0 for numerical simulations. We find that the difference in the final temperature profile is negligible between an AVP of 0.1 and 1.0; similarly for AVP’s of 10^{-4} and 0. However, the average temperature is 20 – 30% larger in the higher AVP case. Fig. 4 shows the evolution of density, temperature and L_X from these set of simulations. In keeping with the recommended value for AVP, we chose an AVP= 0.5 to run all of our merger simulations. We also ran an equal-mass merger with 10% gas fraction and 0.1 R_{vir} impact parameter with three different AVP’s of 0.1, 0.5 and 1.0. The results are indistinguishable between the three, showing that we are in a convergent regime for this physically reasonable value of AVP= 0.5.

2.4 Merger Orbits

Cosmological simulations of large-scale structure formation shows that $\sim 40\%$ of the mergers occur with an eccentricity $e = 1.0 \pm 0.1$ and $\sim 85\%$ have an impact parameter $b > 0.1 R_{\text{vir}}$ (Khochfar & Burkert 2006; Benson 2005). More than 50% of the mergers occur with $b > 0.5 R_{\text{vir}}$. Keeping these larger impact parameters in mind, we create three orbits with $b = 0.01, 0.1$ and $0.5 R_{\text{vir}}$; – two of our three orbits probe the larger impact parameters. We chose elliptical orbits with $e \sim 0.05, 0.2$ & 0.45 . We also have a suite of equal-mass hyperbolic mergers. Our simulations contain a set of 27 elliptical and 9 hyperbolic orbits, for a total of 36 simulations. Table 3 lists the eccentricity, total energy and the initial velocities for each merger simulation.

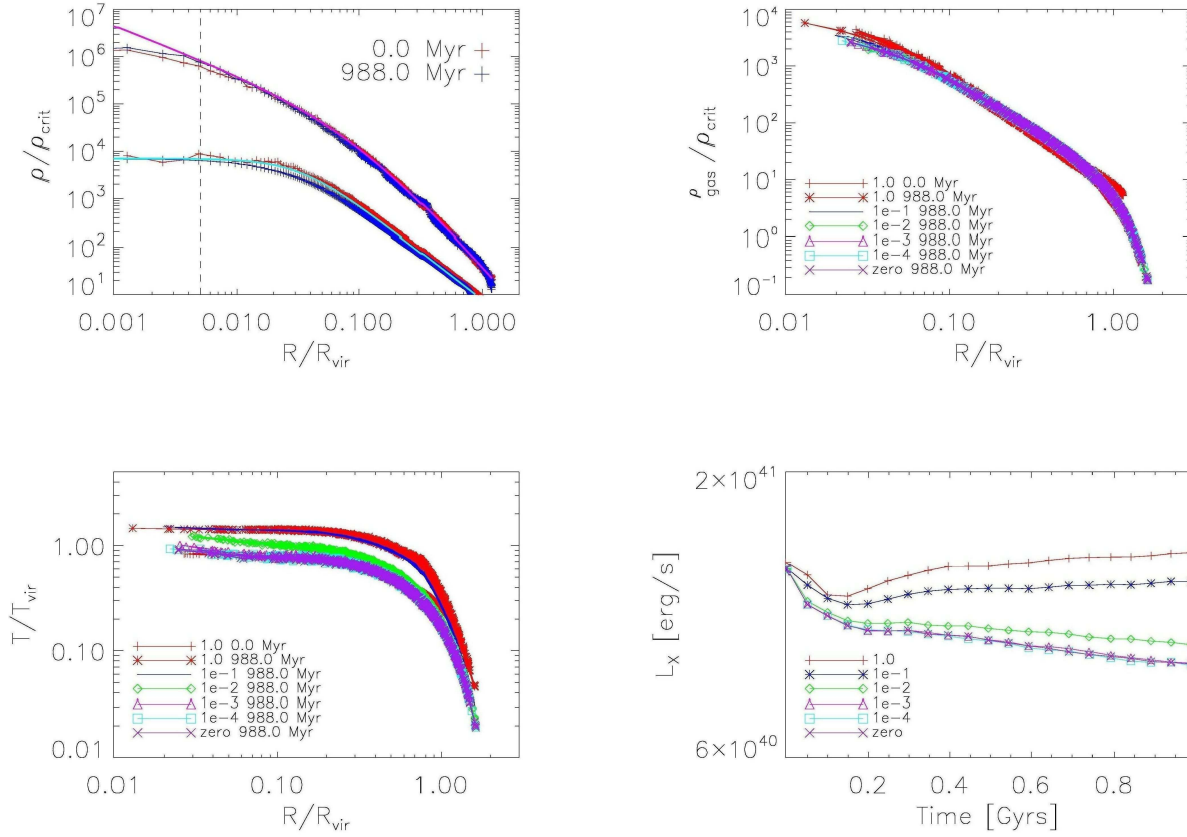


Figure 4. *Top Left:* The gas (lower curve) and dark matter (upper curve) density profile with the analytical β and the NFW profile overlaid as solid lines, for the primary galaxy with gas fraction of 10%. The galaxy is represented by 5×10^5 dark matter and gas particles each and is evolved for 1 Gyr with an AVP= 0.1. The flattening of the dark matter profile occurs in the inner regions of the halo and corresponds to the softening – represented by the vertical dashed line. *Top Right:* The same plot showing the gas density profile at 1 Gyr for different AVP’s. *Bottom Left:* The evolution of the temperature profile for different AVP’s. The temperature increases by almost a factor of 2 for AVP > 0.01. *Bottom Right:* The evolution of the total X-ray emission via thermal bremsstrahlung from gas particles with $T > 10^{5.2}K$ and $\rho < 0.01 M_{\odot}/pc^3$.

Table 3: The list of all the merger simulations performed. The first three 1:1 mergers for each gas fraction are the hyperbolic encounters, while the rest are all bound elliptical orbits with a fixed orbital energy for a given merger ratio.

Gas	Merger Type	b	Eccentricity	Orbital Energy	Primary Vel.	Secondary Vel.
-	-	[kpc]	-	[10^{56} erg]	[km/s]	[km/s]
1% gas	1:1	2.3	2.99	2864.6	137.8	137.8
	1:1	22.8	2.95	2864.6	137.8	137.8
	1:1	114.3	2.78	2864.6	137.8	137.8
	1:1	2.3	0.06	-1432.3	68.9	68.9
	1:1	22.8	0.18	-1432.3	68.9	68.9
	1:1	114.3	0.41	-1432.3	68.9	68.9
	3:1	1.9	0.06	-542.0	29.5	92.2
	3:1	19.4	0.20	-542.0	29.5	92.2
	3:1	96.8	0.44	-542.0	29.5	92.2
	10:1	1.7	0.07	-188.5	10.5	108.9
	10:1	16.7	0.21	-188.5	10.5	108.9
	10:1	83.7	0.48	-188.5	10.5	108.9
10% gas	1:1	2.3	2.99	3397.9	143.9	143.9
	1:1	22.8	2.95	3397.9	143.9	143.9
	1:1	114.3	2.78	3397.9	143.9	143.9
	1:1	2.3	0.05	-1698.9	71.9	71.9
	1:1	22.8	0.18	-1698.9	71.9	71.9
	1:1	114.3	0.41	-1698.9	71.9	71.9
	3:1	1.9	0.06	-642.9	30.8	96.3
	3:1	19.4	0.20	-642.9	30.8	96.3
	3:1	96.8	0.44	-642.9	30.8	96.3
	10:1	1.7	0.07	-223.6	10.9	113.6
	10:1	16.7	0.21	-223.6	10.9	113.6
	10:1	83.7	0.48	-223.6	10.9	113.6
18% gas	1:1	2.3	2.99	3910.1	149.0	149.0
	1:1	22.8	2.95	3910.1	149.0	149.0
	1:1	114.3	2.78	3910.1	149.0	149.0
	1:1	2.3	0.05	-1955.1	74.5	74.5
	1:1	22.8	0.18	-1955.1	74.5	74.5
	1:1	114.3	0.41	-1955.1	74.5	74.5
	3:1	1.9	0.06	-739.8	31.9	99.7
	3:1	19.4	0.20	-739.8	31.9	99.7
	3:1	96.8	0.44	-739.8	31.9	99.7
	10:1	1.7	0.07	-257.3	11.3	117.6
	10:1	16.7	0.21	-257.3	11.3	117.6
	10:1	83.7	0.48	-257.3	11.3	117.6

3 ANALYSIS

3.1 Calculating X-ray emission

We assume that the primary source of X-rays in a galaxy merger is thermal bremsstrahlung from hot, diffuse gas of primordial composition. In real galaxies, X-rays are also produced by discrete sources like supernova remnants, compact binary objects as well as accretion events occurring around massive black holes. However, such emission is more likely to occur in the denser central regions of the galaxy and hence, also more likely to be obscured by the larger column density of the intervening gas and dust. The hot, diffuse gas should be relatively less affected by in situ absorption (Cox et al. 2006). Following Cox et al. (2006), we identify only those particles that have $T > 10^{5.2} K$ and density $\lesssim 0.01 M_{\odot} \text{pc}^{-3}$ as X-ray emitting hot, diffuse gas. Throughout this paper, we will use the term hot gas to denote those gas particles that satisfy this criteria. Therefore, we estimate the X-ray luminosity as:

$$L_X = 1.2 \times 10^{-24} (\mu m_p)^{-2} \sum_i m_i \rho_i T_i^{1/2} \text{erg s}^{-1}, \quad (4)$$

where m_p is the mass of a proton, m_i, ρ_i, T_i is the mass, density and temperature of a gas particle respectively and the summation is over only the hot gas particles.⁴

The orbital energy in the gas is $\gtrsim 10^{58}$ erg; much of this energy gets redistributed as the internal kinetic energy of the remnant. The average X-ray luminosity in all the simulations is $\sim 10^{41}$ erg/s and it would take more than 10 Gyrs to radiate away only the orbital energy via bremsstrahlung. To ensure that we select only those gas particles that will remain hot, we compute the cooling times for the hot gas particles and reject the ones that have cooling time less than the dynamical time. As a further safeguard, we also reject the hot gas particles that have a cooling time less than the time between consecutive snapshots (~ 100 Myrs for all simulations). After these two step rejection process we recompute the X-ray emission from the hot gas and the shocked gas particles and find that the X-ray emission changes by less than 5% for the hot gas and less than 1% for the shocked gas particles. Thus, our predictions regarding X-ray emission from the hot and the shocked gas are not susceptible to significant changes from radiative losses.

⁴ Note that enriched gas at $\sim 10^6$ K will cool primarily through metal line emission, implying that the X-ray emission could well be enhanced in actual colliding galaxies.

3.2 Shock Detection

In our simulations, large-scale shocks develop in the gas. Since our simulations are adiabatic, shocks are the only mechanism that can increase the entropy of a gas particle. We take advantage of the conservative-entropy formulation (Springel & Hernquist 2002) of GADGET-2 (Springel 2005) to identify the shocked particles based on their rate of entropy change. Each snapshot file in GADGET-2 gives the rate of change of entropy for every gas particle. We set a threshold for identifying shocked gas particles. We chose the threshold conservatively, i.e., we are likely to miss some shocked particles. The threshold, in code units, is 10^{10} , 3×10^9 and 2×10^9 for 1%, 10% and 18% gas fractions respectively. We also locate every particle that was ever shocked by analysing all the snapshots and tracking the particle ids. This helps to determine the mechanism behind a particle's unbinding.

3.3 Unbound particles

At the beginning of the simulation, we identify the most bound 10% of the particles of each galaxy and track them to follow the centre of mass. The centre of mass velocity is subtracted to compute the total energy of individual particles. Particles that have a total energy greater than zero are considered unbound from the system. By defining the unbound material in this fashion, we avoid tagging particles that could be unbound from each galaxy but not unbound from the entire system. In the simulations where we have a merger remnant, we identify the unbound particles at the end of the simulation (when the system has settled down) and track those particles through the duration of the merger.

4 RESULTS

In this section we explore how different merger ratios, gas fractions and impact parameters affect the X-ray emission and the unbound gas. A priori, we expect to find an increasing trend for X-ray emission with increasing progenitor masses – this is due to the higher virial temperature and larger hot gas fraction in the more massive haloes (see Table 4). In addition, a smaller impact parameter implies denser parts of the galaxy inter-penetrate; this should lead to stronger shocks and larger hot gas fractions. Therefore we expect the X-ray emission from both the regular hot gas component and the shocked component to increase with a decreasing impact parameter. A larger impulse is delivered during a close encounter with more massive galaxies; therefore, we expect an increasing trend in the unbound gas fractions with increasing galaxy mass and decreasing impact parameter. Thus, both L_X and the unbound gas fraction should behave in an analogous manner; we test these hypotheses in this section.

4.1 X-ray emission

Though the isolated galaxies have varying initial hot gas fractions, during the course of the merger more than 90% of the gas is in the hot phase. This is caused primarily by shock heating during the encounter. For example, the smallest secondary galaxies have $\sim 40\%$ of their gas in the hot phase in isolation (see Table 4), but that fraction increases to more than 90% during the merger process. The total X-ray luminosity of the merger is determined by this hot gas fraction and can be seen from the correlated decrease in both the hot gas fraction and the X-ray luminosity (see Fig. 5 and Fig. 6).

For equal-mass mergers, the elliptical and hyperbolic orbits produce a peak L_X of $\sim 10^{40}$ erg/s for the 1% gas fraction. This is from the first pericentre pass, which creates the strongest compressive forces. Since L_X is proportional to the square of the density, the shocks at this stage create the largest X-ray emission. However, note that even though we are talking about close passages, the average distance between the centres is greater than 20 kpc, greater than the typical disk size in spiral galaxies. Hence, the shocks will be observed at large distances from the centres. For equal-mass mergers with 10% gas, L_X peaks at $\sim 8 \times 10^{41}$ erg/s during pericenter pass. The 18% gas fraction simulations produce L_X as high as $\sim 2 \times 10^{42}$ erg/s.

The simulations with the smallest impact parameters cause the denser parts to collide. As the impact parameter increases to $0.5 R_{\text{vir}}$, the lower density regions of the galaxy inter-penetrate. Since our simulations are adiabatic, the maximum increase in the density can be a factor of 4; the strong dependence of L_X on the gas density results in a lower L_X .

The equal-mass mergers create the strongest shocks in our entire suite of simulations. However, the surprising part is that the strongest temperature enhancements occur after the galaxy centres have passed by. At this point the shocked material encounters a lower density material upfront and accelerates forward. The material in the far side of the galaxy is still continuing in orbit with a velocity opposite to that of the accelerated shocked material. When these two fluids collide, the strongest shocks (measured by the rate of entropy change) are produced (see Fig. 7 and 8). This can also be seen from the temperature projections in Fig. 9 where the highest temperatures are created by the gas that is thrown forward after the pericenter passage, colliding with the gas in the far side of the galaxy. Consequently, the peak L_X from shocks occurs some time after the peak L_X . The equal-mass mergers with 1%, 10% and 18% gas have a peak L_X from shocks of $\sim 10^{37}$, $\sim 10^{39}$ and $\sim 3 \times 10^{39}$ erg/s.

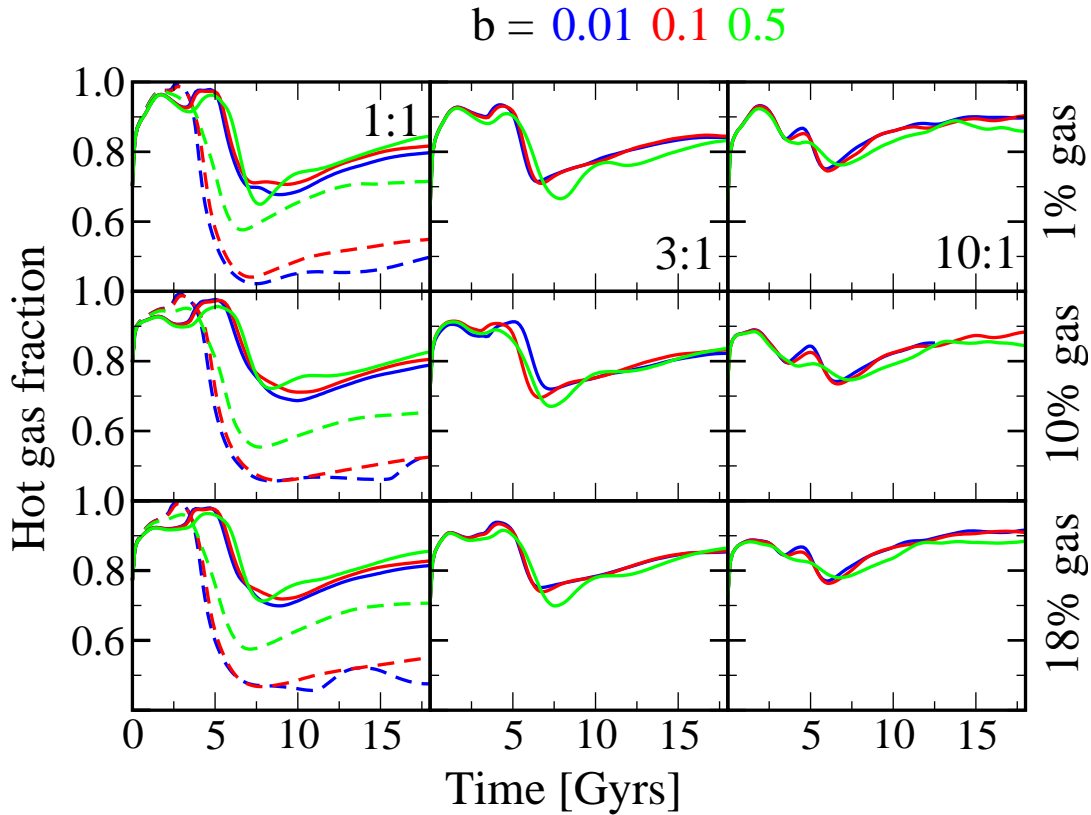


Figure 5. The evolution of the hot gas fraction for all the 36 simulations. The left column contains 1:1 mergers, the middle column contains 3:1 mergers and the right column contains the 10:1 mergers. The top row, middle and the bottom row show simulations with 1%, 10% and 18% gas fractions respectively. The blue, red and the green shows the 0.01, 0.1 & 0.5 R_{vir} impact parameters respectively. The dashed lines in the left column show the hyperbolic 1:1 mergers. We see that the peaks of the hot gas fractions corresponds to the pericenter passages. The most drastic evolution is seen in the equal-mass mergers where hot gas fraction evolves from $\sim 80\%$ to $\sim 50\%$ for 0.01 and 0.1 R_{vir} . For all the other simulations the final hot gas fraction reaches equilibrium at around 80%.

The 3:1 mergers show a similar pattern; with L_X increasing with decreasing impact parameter and increasing gas fraction. The peak L_X for the 3:1 mergers with 1% gas is $\sim 10^{39}$ erg/s while the peak L_X from shocks is $\sim 5 \times 10^{36}$ erg/s. The 10% gas fraction produces a peak L_X of $\sim 10^{41}$ erg/s and $\sim 10^{38}$ is from shocks. For the 18% gas fraction, the peak L_X and the peak L_X from shocks are $\sim 10^{42}$ and $\sim 10^{39}$ erg/s respectively. Though peak L_X from shocks is larger than 10^{39} erg/s it is still 3 orders of magnitude smaller than the total L_X signature from the merger event.

The 10:1 mergers follow the trend and for the 1% gas fraction simulations the peak L_X and the peak L_X from shocks are $\sim 2.0 \times 10^{39}$ and $\sim 10^{36}$ erg/s respectively. For the 10% simulations the peak L_X is $\sim 2 \times 10^{41}$ erg/s while the peak L_X from shocks is $\sim 3 \times 10^{37}$ erg/s. For the 18% gas fractions, the peak L_X is $\sim 5 \times 10^{41}$ erg/s while the peak L_X from shocks is $\sim 2 \times 10^{38}$ erg/s. Clearly, the 10:1 mergers do not produce any appreciable X-ray signature from the shock-heating of the hot gas even with the largest gas fractions. See Table 6 for detailed data on X-ray production for all the simulations.

From our simulations, we see that the expected trends do occur. The X-ray luminosity, both intrinsic and from shocks, increases with increasing halo mass and decreasing impact parameters. Larger initial velocities do generate larger L_X ; however, if the hot gas fraction drops too much, as it does in the case of some of the hyperbolic mergers, the X-ray emission can be reduced. In light of these trends, the best bet to detect the shock signature of hot halo gas during mergers would be to locate major mergers between Milky Way-type galaxies that are happening in the local universe. Such a system would produce significant X-rays from the hot halo and the shock-heated interface if the galaxies are to be observed in the initial stages of the merger. Spatial resolution will not be an issue since the signature is an extended source; the problem would be the identification of the underlying shock X-ray emission and separate it from the emission from the hot halo particles themselves. *XMM-Newton*, with its superior collecting area, would have been the instrument of choice; however, the inferior sensitivity of *XMM-Newton* in the soft X-ray band, where most of the shocked gas in our simulation radiates (the maximum temperature reached in our simulations is ~ 0.3 keV), *Chandra* is best suited to characterise the hot halo gas. Our threshold for the X-ray flux, 10^{-15} erg/s/cm² is relevant to *Chandra*.

So far we have discussed the production of X-rays by the merger, both from the hot gas in the halo and the shocks. We

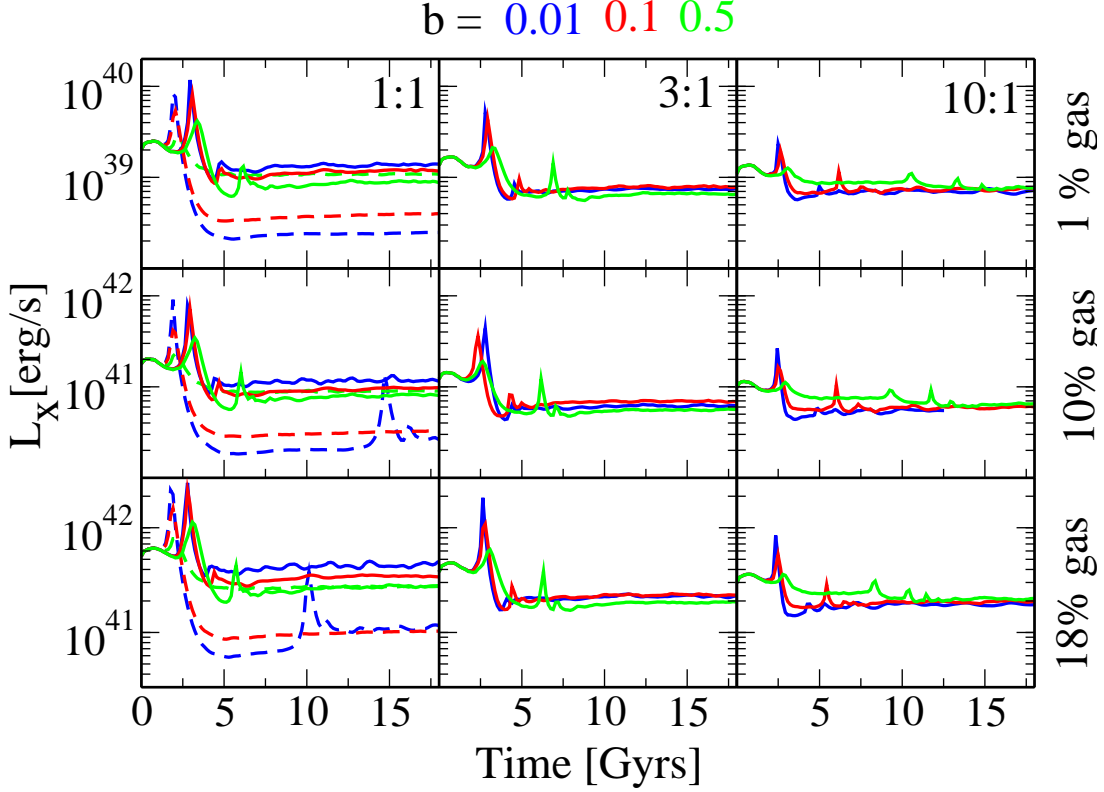


Figure 6. The X-ray luminosity versus time for all simulations. The peak X-ray luminosity increases with increasing gas fraction $\propto \rho_{\text{gas}}^2$ and occurs at the first pericentre pass. The peak X-ray luminosity also shows an increasing trend with decreasing impact parameter and decreasing secondary galaxy mass, correlated with the amount of shock heating that occurs. The line types and the colours are the same as in Fig 5.

found that the X-ray emission depends on a variety of parameters like the merger ratio, the cumulative mass, the merger orbit and the gas fraction in the simulation. We attempt to combine the effects of all these factors to predict the peak X-ray luminosity from shocks as a function of the gravitational impulse from the merger. Covington et al. (2008) derive an empirical fitting formula for the impulse motivated by numerical simulations of galaxy mergers. The impulse, ΔE , is approximated by:

$$\Delta E \propto \frac{G^2 M_1 M_2^2}{v_p^2 [r_p^2 + r_p \times R_{\text{vir},1}]}, \quad (5)$$

where M_1 is the primary galaxy mass, M_2 is the mass of the secondary, v_p and r_p are the relative velocity of the galaxies and the pericenter distance as determined from the simulation.

We also define a “merger strength”, H , that is logically related to L_X . L_X depends on $\rho^2 \sqrt{T}$, and $T \propto v_{\text{relative}}^2$ (see Eqn. 1). Therefore, L_X should depend on v_{relative} ; we use the velocity at perihelion, v_p determined from the simulation to capture this. Our final equation for the merger strength, ΔH , is then $\Delta E f_{\text{gas}}^2 v_p$, and can be written as:

$$\Delta H \propto \frac{G^2 M_1 M_2^2 f_{\text{gas}}^2}{v_p [r_p^2 + r_p \times R_{\text{vir},1}]}, \quad (6)$$

We then fit the peak L_X from shocks, L_{peak} , as a linear function of ΔH . However, a better fit, with a correlation co-efficient of 0.96, is obtained with a logarithmic fit. The fit for our set of 36 simulations is:

$$\log_{10} \left[\frac{L_{\text{peak}}}{10^{38} \text{ erg/s}} \right] = 0.88 \times \log_{10} \Delta H - 1.25. \quad (7)$$

This fit captures essential physics in a gas-rich galaxy merger and can be used to estimate the peak L_X from shocks in a merger (see Fig. 10). Such a fit is quite useful in modelling the total L_X from shocks in semi-analytic studies of galaxy formation.

4.2 Unbound Gas

To constrain the amount of unbound material resulting from the mergers, we evolve the corresponding initial conditions in isolation for a similar time-scale. Every galaxy will lose some small amount of material from spurious two-body relaxation,

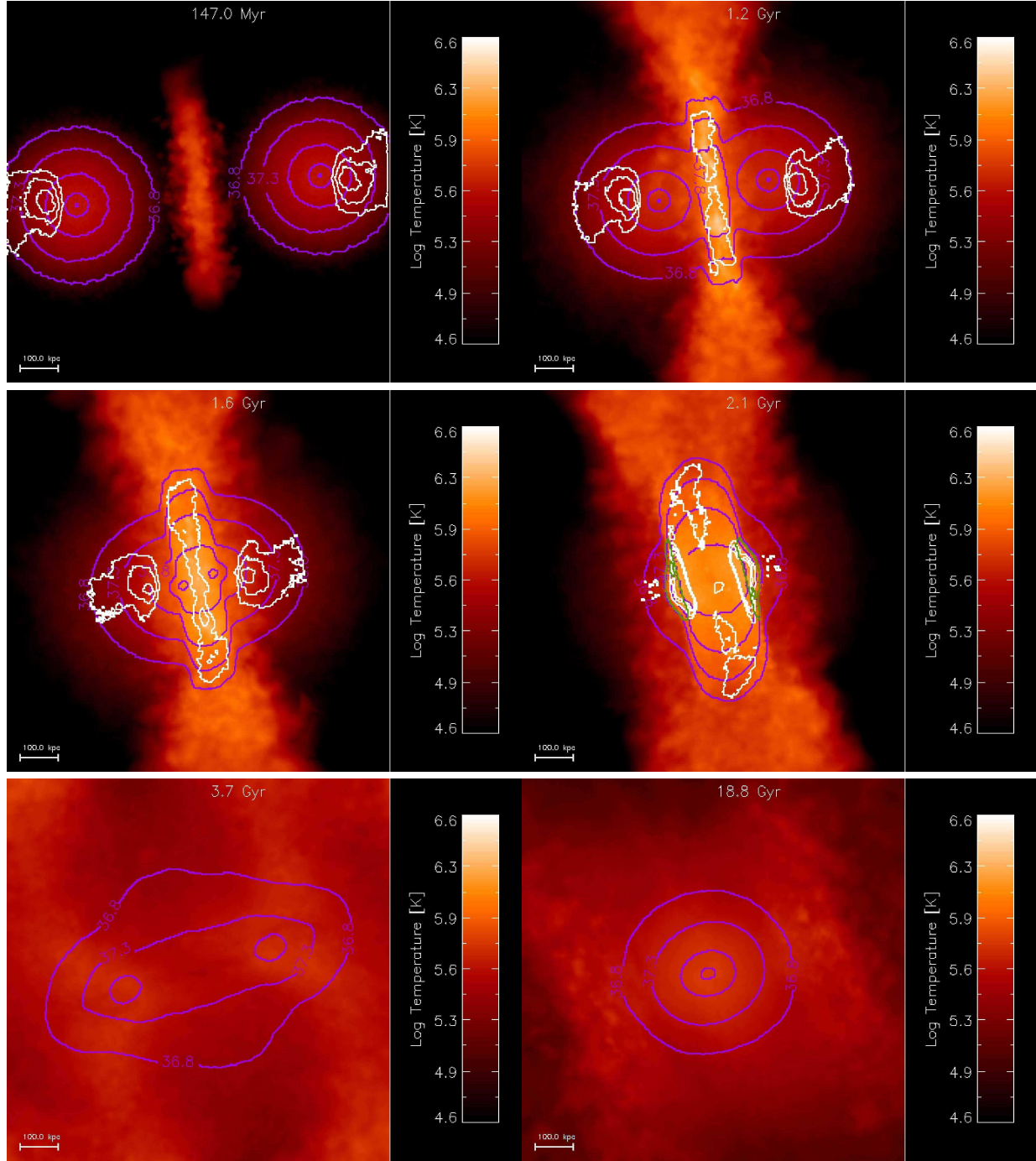


Figure 7. Temperature projection for the 18% gas fraction for a hyperbolic equal-mass merger with an impact parameter of 2.3 kpc. This run has the highest X-ray emission and largest unbound material. The X-ray contours are shown in purple, the unbound material with white contours and the portion of unbound material that is shocked with green contours. The shocked unbound only shows up in the 4th image. The unbound material is identified at the end of the simulation and then traced through the entire run. Most of the unbound material comes from two distinct regions: the far lobes of the galaxy and the shocked front in between the galaxies. The projected X-ray emission also exceeds 10^{38} erg/s in the shocked region with a total shocked X-ray emission exceeding 10^{40} erg/s.

and by evolving the galaxies in isolation, we can estimate the magnitude of this effect. We deduct this amount of unbound material (column 3 in Table 4) when we compute the final unbound fraction from the merger (see column 4 in Table 5).

Table 4: Isolated galaxy evolution. We evolve isolated galaxies with AVP= 0.5 for $\gtrsim 10$ Gyr to ascertain the amount of unbound material from internal processes. This fraction is subtracted from the unbound material from the mergers, we can fix the actual amount freed during the merger itself.

Gas Content	Galaxy Type	Unbound gas	L_X	R_{vir}	M_{vir}	Hot gas
–	–	[%]	[10^{40} erg/s]	[kpc]	[$10^{10} M_\odot$]	[%]
1% gas	Primary [†]	0.43	0.09	214.8	113.2	93.2
	Onethird	0.69	0.03	149.1	37.8	73.4
	Onetenth	0.84	0.01	100.2	11.5	41.3
10% gas	Primary [‡]	0.60	8.46	212.9	110.2	89.8
	Onethird	0.61	3.38	149.1	37.7	75.9
	Onetenth	0.83	0.94	100.7	11.7	45.3
18% gas	Primary	0.72	27.5	213.9	112.0	95.2
	Onethird	0.60	11.3	148.6	37.6	79.0
	Onetenth	0.76	3.05	100.7	11.6	48.4

We find that most of the unbound material originates at or near the virial radius of the respective galaxies. As the merger progresses, this material escapes to beyond $3 R_{vir}$ even before the second passage. By the end of the simulation, this unbound gas is far ($\gtrsim 1$ Mpc) from the remnant (see Fig. 7), thereby alleviating the problem of transporting gas to inter-galactic distances (Ferrara et al. 2000). We find that $\sim 9\%$ of the gas unbinds, along with a similar fraction in the dark matter. Per merger, this translates to a gas mass $\gtrsim 3 \times 10^{10} M_\odot$ from equal-mass and $\gtrsim 10^{10} M_\odot$ from 3:1 mergers flowing into the IGM (see Fig. 11). While at 18 Gyrs our simulation lasts much longer than a Hubble time, nearly all the unbound material flows outside $3 R_{vir}$ within the first 5-6 Gyrs. Considering that every galaxy has had a major merger in the past (Conselice et al. 2003, see), this may be an excellent mechanism to enrich the IGM. Thus galaxy mergers play an important role not only in the evolution of the galaxies and hierarchical structure formation, but they may also influence both the mass and the metallicity content of the IGM.

We find that the unbound material originates from two distinct regions – from the near and far lobes of the galaxy along their line of motion. These constitute the regions that are shocked during the course of the merger. The near lobes are shocked before pericenter passage, which can be seen in Fig. 7. These shocked gas particles then leave in directions perpendicular and away from the direction of the motion of the galaxies as they expand into the lower density regions. Their escape is facilitated by the lower density and pressure of the ambient medium above the shocked region and can be seen from the velocity vectors of the unbound particles pointing outwards in Fig. 8. The gas particles from this region escape from the galaxies the earliest.

To understand why the gas escapes from the far regions of the galaxies, we must look into the shock process itself. As the galaxies pass through pericenter, the density in front of the shocked material suddenly drops rapidly. This causes the shocked material to accelerate, and it is flung forward. However, the material at the far side of the galaxy is still moving with the bulk flow. This naturally results in the largest relative velocity and hence, the strongest shocks in the simulation. The original shocked gas interacts with the gas from the far side, and the gas from the far side receives a large impulse, which causes the gas to flow outward instead of continuing with the bulk motion of its host galaxy. This material can be seen as the brightest patches in the temperature images (see Fig. 8 and 9). In unequal-mass mergers, the impulse affects the lower mass galaxies more, and an asymmetry is introduced whereby the strongly-shocked unbound material comes primarily from the smaller galaxy. This can be seen in the images of the temperature projections for the unequal-mass mergers where the brightest patches are towards the side of the smaller galaxies (see Fig. 9 for the 3:1 case). Although most of the unbound material originates from a radius greater than $0.5 R_{vir}$ in each galaxy and therefore should have a systematically lower metallicity, the gas can get enriched during the merger process itself from starburst-driven winds.

[†] at 15 Gyrs.

[‡] at 10 Gyrs.

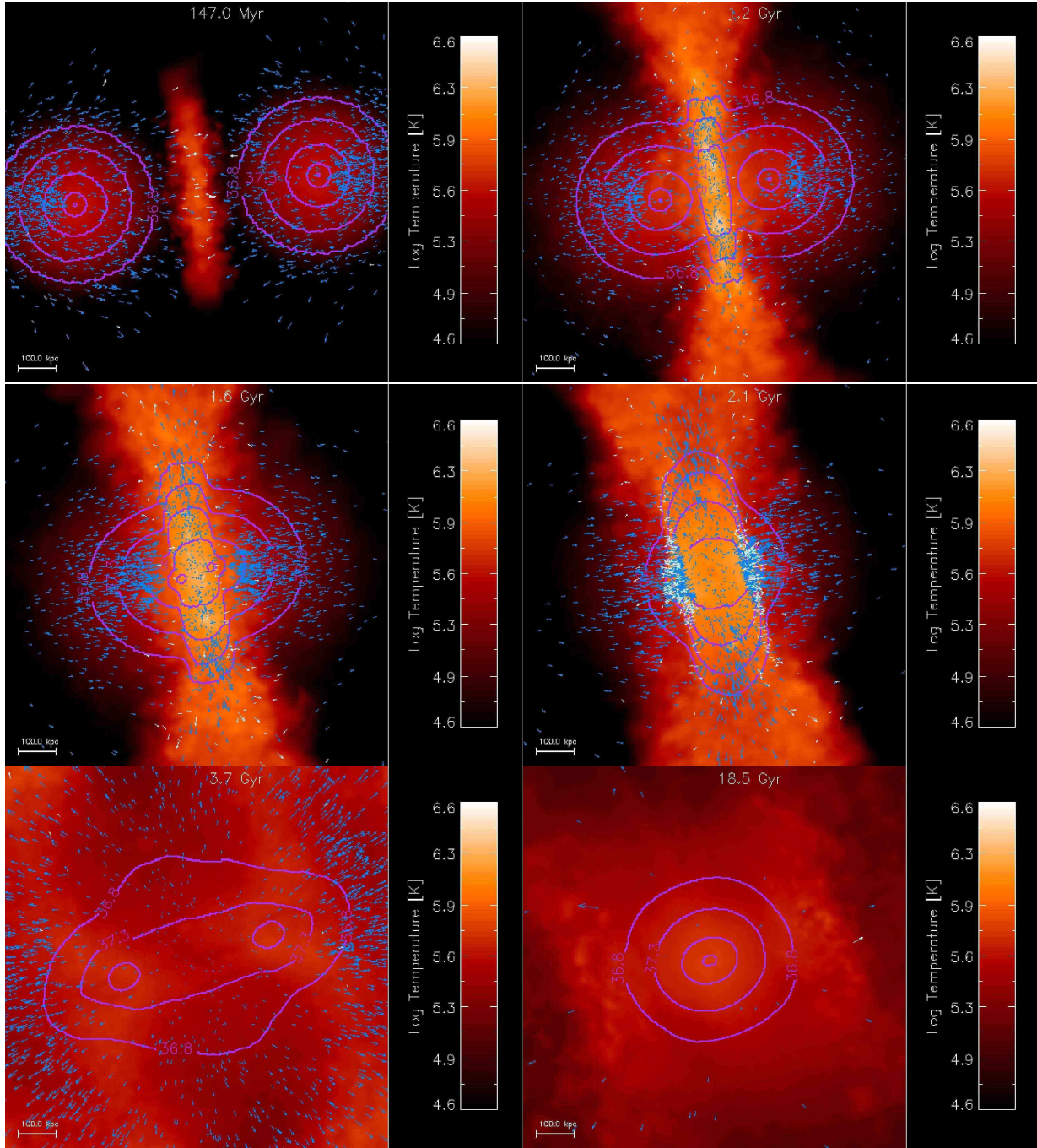


Figure 8. Temperature projections for the 18% gas fraction for a hyperbolic equal-mass merger with an impact parameter of 2.3 kpc. This run has the highest X-ray emission and largest unbound material. The velocities of a fraction of randomly chosen unbound particles is plotted; blue represents unshocked unbound material while white shows the shocked unbound material. We see that the unbound material escapes preferentially along the shocked front away from the plane of the merger since this provides the least resistance in terms of gas pressure. Strong shocks are generated once the centres have passed and material is ejected that interacts with the bound material at the other end of the galaxy that is yet to make a close pass (and hence has a velocity vector opposite to that of the unbound material). This is seen in the right image in the middle row. All of the unbound material leaves the vicinity of the galaxy much before they actually merge ($\lesssim 6$ Gyrs).

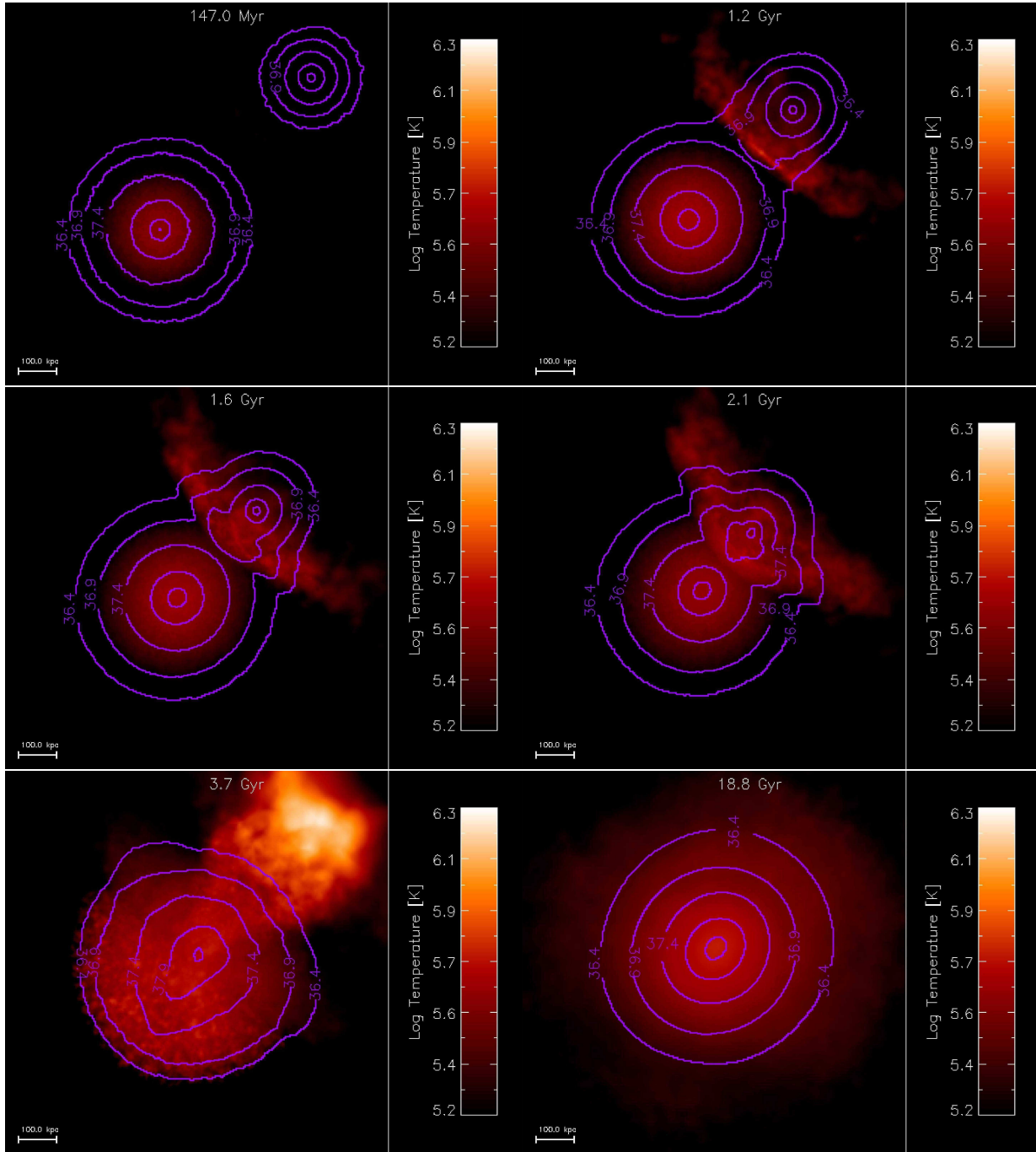


Figure 9. Projected temperature and L_X contours for a 3:1 merger with 18% gas fraction and an impact parameter of 1.9 kpc. A prominent bow shock develops as the secondary galaxy passes through the halo of the primary. Even at 2.2 Gyr, when the centres are separated by ~ 100 kpc, the strong shock persists and can be easily seen in the temperature map. Once the secondary material passes by the primary centre, a lot of material is ejected that gets shock-heated by the secondary galaxy as it moves inwards along the orbit. This can be seen in the patch of very bright material in the left-bottom image. The final image at 18.8 Gyr shows the merger remnant completely relaxed with spherical L_X contours. The minimum value of the L_X contour is $10^{36.4}$ erg/s and increases in factors of $10^{0.5}$ erg/s.

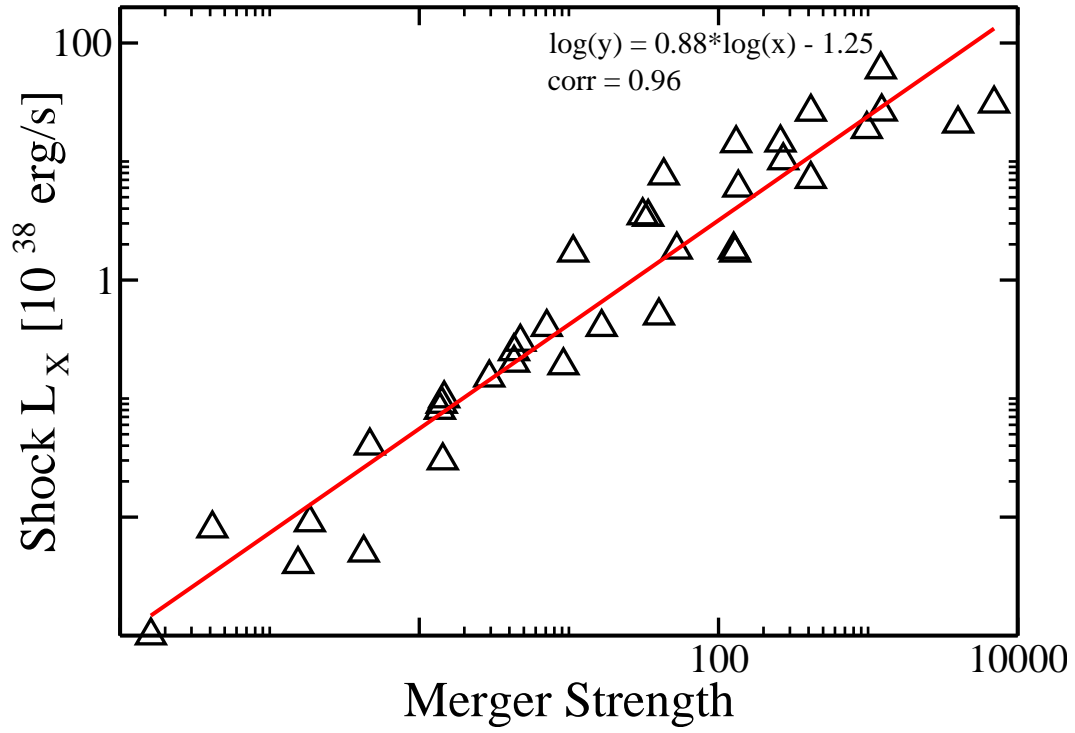


Figure 10. The fit for the peak L_X from shocks as a function of the the merger strength, ΔH (see Eqn. 6). Each simulation is plotted as a triangle while the fit (see Eqn. 7) is plotted with a red line. The correlation for this fit is 0.96 and implies that Eqn. 7 is a good linear fit.

Table 5: Unbound gas from mergers. The first three equal-mass mergers for each gas fraction are the hyperbolic encounters while the rest are all bound elliptical orbits with a fixed amount of energy in the orbit for a given merger ratio. The unbound fraction (Column 4) is obtained by deducting the unbound gas fractions when evolved in isolated (see Table 4) from the fraction determined at the end of the simulation. Column 5 shows the fraction of all the gas particles that are shocked during the simulation. The unbound gas particles are tracked through the snapshots to find where they become unbound or shocked. The fraction of unbound gas particles that are shocked during the simulation is shown in Column 6.

Gas	Merger Type	b [kpc]	Unb. frac. [%]	Shocked (all) [%]	Shocked (unb) [%]
1% gas	1:1h	2.3	19.2	13.1	49.6
	1:1h	22.8	18.5	11.1	46.7
	1:1h	114.3	11.2	5.9	44.1
	1:1	2.3	9.4	14.1	84.2
	1:1	22.8	8.4	13.8	85.8
	1:1	114.3	5.9	11.9	89.5
	3:1	1.9	6.7	9.4	69.6
	3:1	19.4	5.7	9.2	73.1
	3:1	96.8	4.1	8.0	80.0
	10:1	1.7	1.2	2.6	60.9
	10:1	16.7	1.1	2.5	62.6
	10:1	83.7	1.2	4.0	66.0
10% gas	1:1h	2.3	23.8	22.5	53.6
	1:1h	22.8	20.0	13.4	53.4
	1:1h	114.3	16.2	8.4	44.8
	1:1	2.3	9.7	14.6	86.9
	1:1	22.8	8.9	14.1	86.8
	1:1	114.3	6.4	12.1	87.7
	3:1	1.9	6.8	9.1	67.2
	3:1	19.4	5.5	7.2	63.6
	3:1	96.8	3.7	6.0	68.5
	10:1	1.7	0.8	1.4	41.0
	10:1	16.7	0.9	1.2	36.4
	10:1	83.7	1.0	2.0	39.6
18% gas	1:1h	2.3	21.8	19.8	50.7
	1:1h	22.8	17.5	12.2	52.5
	1:1h	114.3	11.1	7.0	50.8
	1:1	2.3	8.6	13.7	85.0
	1:1	22.8	8.1	13.6	85.6
	1:1	114.3	5.6	11.6	88.9
	3:1	1.9	6.0	8.2	67.8
	3:1	19.4	5.3	7.8	70.2
	3:1	96.8	3.9	6.7	77.5
	10:1	1.7	1.1	2.0	44.7
	10:1	16.7	1.0	1.9	46.2
	10:1	83.7	1.1	2.8	54.4

It is clear that the unbound material is related to the extensive shocks in our simulations. Here, we attempt to disentangle the effects of the dynamics and the hydrodynamics of the gas as it unbinds. We backtrack the unbound material at the end of the simulation through the snapshots to identify when the gas particle first unbinds. At the same time, we note when and if the gas particle is shocked. Table 5 shows the results of this process. We find that for equal-mass mergers, galaxies on hyperbolic orbits systematically show that a smaller fraction of the unbound material originates from shocks, compared to galaxies on elliptical orbits. This may be because galaxies on hyperbolic orbits only undergo one pericenter pass, while galaxies on elliptical orbits experience multiple pericenter passes (and shocks). Elliptical orbits show a strong correlation between unbound and shocked particles. For instance, for equal-mass mergers, $\sim 85\%$ of all the unbound particles were shocked during the simulation. By tracking the particles back, we find that the overwhelming majority of gas was unbound right after being shocked.

In a similar spirit as the previous estimation of the peak L_X from shocks, we quantify the effect of the orbit on the unbound material. We follow the formulation of Covington et al. (2008) and use the impulse formulated in Eqn. 5. A linear regression analysis on f_{unb} and ΔE and obtain a linear relationship of the form:

$$f_{\text{unb}} = 3.14 \times \log_{10} \Delta E - 0.16. \quad (8)$$

The correlation coefficient for this fit is 0.95 (see Fig. 12), implying that the two quantities are well described by a linear function. Because we started out on a physically motivated basis by equating the impulse with the unbound fraction, this high correlation points to an underlying relation between the impulse and the unbound fraction. Since most of the hyperbolic mergers do not leave a remnant and the 10:1 mergers have only 1% unbound gas,, we do not use those simulations to fit this equation. Thus, out of our total 36 simulations, we have used only the 18 1:1 and 3:1 with elliptical orbits to obtain Eqn. 8.

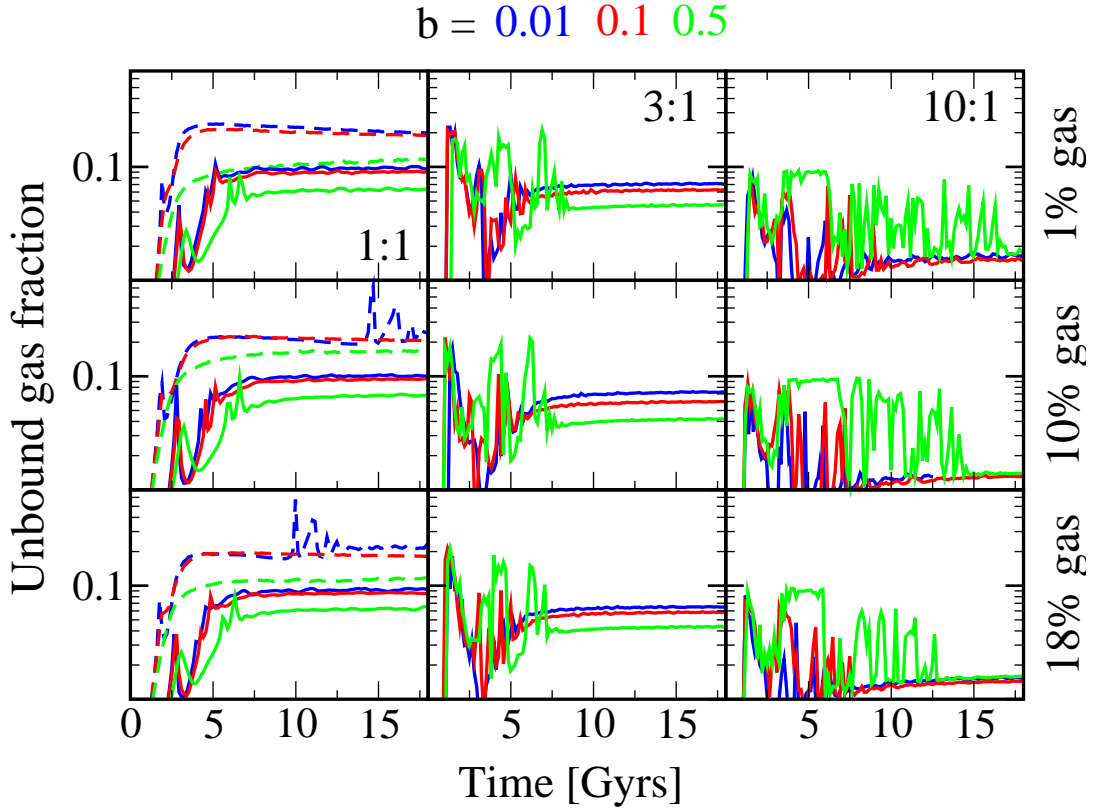


Figure 11. Evolution of the unbound gas fraction for all simulations. Equal-mass mergers with the 0.01 & 0.1 R_{vir} has $\sim 20\%$ unbound gas fraction from the final merger remnant. The 3:1 mergers release about 5-7% gas while the 10:1 mergers unbind the least amount of gas at about 0.5%. The irregular nature of the unbound gas fraction for the 3:1 and the 10:1 mergers is caused by the multiple passages taken by the secondary galaxy.

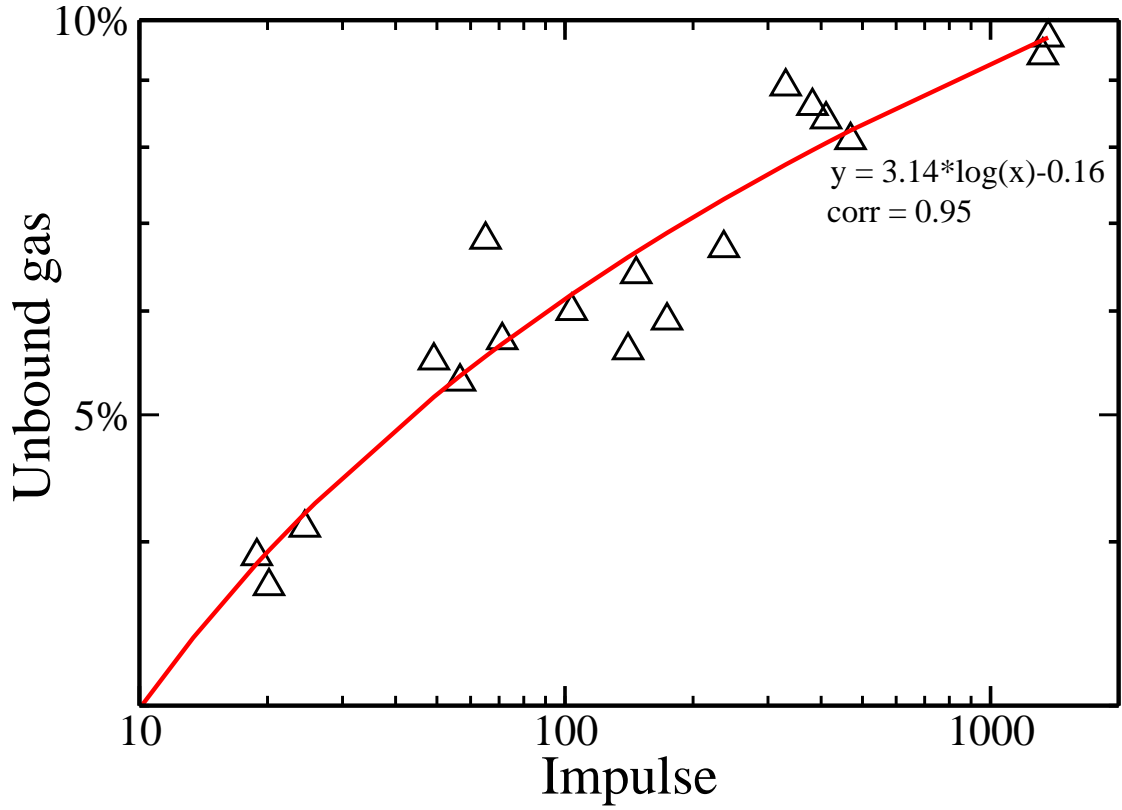


Figure 12. The linear fit (red) for the unbound fraction and the impulse, ΔE (see Eqn. 5). We only use the 18 simulations with the 1:1 and 3:1 bound orbits since they leave a merger remnant in all cases and have unbound fractions $> 3\%$. We will explore this in an accompanying paper to find the unbound gas fraction throughout the history of structure formation.

Table 6: Characteristics of the merger simulation and the final remnant for all the simulations. Lack of an entry implies that the merger was not completed within a Hubble time.

Gas Content	Peak L_X^\dagger [10^{40} erg/s]	Peak Shock L_X^\ddagger [10^{38} erg/s]	Unb. gas mass [$10^{10} M_\odot$]	Total unb. mass [$10^{10} M_\odot$]	Hot Gas [%]	R_{vir} [kpc]	Gas within R_{vir} [%]	DM within R_{vir} [%]	Remnant L_X [10^{40} erg/s]
1% gas	0.82	0.25	0.57	44.9	51.0	–	–	–	0.03
	0.54	0.09	0.56	17.5	55.2	–	–	–	0.04
	0.27	0.005	0.35	9.3	71.8	–	–	–	0.1
	1.17	0.19	0.29	2.03	80.2	248.1	58.1	58.4	0.13
	0.81	0.15	0.27	1.95	82.1	247.6	59.1	57.8	0.11
	0.42	0.03	0.27	2.6	84.8	246.3	55.2	56.7	0.09
	0.50	0.08	0.14	3.6	84.2	224.4	62.9	65.1	0.07
	0.40	0.04	0.12	2.5	84.6	224.4	62.0	65.2	0.07
	0.20	0.009	0.09	2.9	83.6	222.1	56.8	63.0	0.07
	0.23	0.004	0.03	2.0	90.7	218.9	68.4	72.8	0.07
	0.19	0.008	0.02	1.4	90.3	218.4	67.4	72.1	0.07
	0.13	0.001	0.03	0.02	1.6	85.6	218.4	64.4	72.3
10% gas	90.5	14.4	7.4	33.9	52.6	217.5	25.5	39.1	3.0
	41.7	6.0	6.1	24.5	52.9	–	–	–	3.3
	23.1	0.5	5.1	12.9	59.3	–	–	–	9.0
	79.3	18.7	3.05	4.36	79.4	251.3	53.8	60.4	12.5
	71.9	10.2	2.84	4.16	80.9	248.6	53.3	58.3	9.5
	34.5	1.7	2.06	3.86	83.3	246.7	49.8	57.1	8.1
	44.0	7.6	1.4	4.2	82.2	224.4	56.0	64.9	6.2
	36.0	3.4	1.2	3.3	83.6	225.3	55.3	65.8	6.8
	18.9	0.4	0.84	2.8	84.3	223.9	52.2	64.6	5.6
	26.5	0.4	0.22	2.0	85.2	216.6	58.7	70.4	5.5
	16.4	0.2	0.22	1.4	88.4	217.1	57.7	71.0	5.8
	11.2	0.1	0.23	1.6	84.5	215.7	55.1	69.7	6.4
18% gas	228.2	59.7	11.9	39.4	47.8	223.0	29.1	42.3	10.8
	153.2	26.2	9.7	36.2	55.5	–	–	–	10.3
	78.7	1.8	6.4	14.7	70.8	–	–	–	27.6
	268.3	30.7	5.0	6.1	81.9	250.4	58.2	59.7	44.0
	227.4	26.3	4.7	5.8	83.1	251.8	57.8	60.6	35.0
	113.1	7.1	3.4	4.9	85.9	248.6	54.0	58.3	28.2
	193.5	20.8	2.3	4.7	85.6	224.8	59.5	65.3	22.2
	108.4	14.2	2.1	3.9	86.2	224.4	58.5	65.2	23.2
	61.8	1.8	1.6	3.9	86.7	223.9	54.6	64.6	19.6
	84.5	3.5	0.39	1.9	91.6	218.4	62.6	72.2	18.4
	54.8	1.7	0.38	1.6	90.8	216.6	60.7	70.4	19.3
	35.8	0.3	0.45	2.8	89.1	217.5	58.7	71.5	21.4

 \dagger L_X is calculated by using only the particles that have $T_{\text{gas}} > 10^{5.2}$ K and $\rho < 0.01 M_\odot/\text{pc}^{-3}$.

 \ddagger Shock L_X is obtained by adding the L_X for the particles that exceed a threshold for $\frac{dS}{dt}$. The threshold, in code units, is $10^{10}, 3 \times 10^9$ and 2×10^9 for 1%, 10% and 18% gas fractions.

5 DISCUSSION

In our simulations, we found that the hot halo gas shock-heats to temperatures $\sim 10^{6.3}$ K in equal-mass mergers and $\sim 10^6$ K in unequal-mass mergers. This is reflected in a strong temperature jump in the regions between the two colliding galaxies, well before pericenter passage, and persists until the first pass. The strongest shocks, and correspondingly the largest X-ray luminosities due to shocked gas, are created after the pericenter passage. For gas fractions greater than 10%, this L_X from shocks remains above observable thresholds of $\sim 10^{39}$ erg/s for at least a period of ~ 300 Myrs, and thus should be detectable in ongoing mergers with *Chandra* and *XMM-Newton*. Compared to the merger timescale, an observable X-ray shock is ~ 20 times shorter. During the merger, the hot gas itself also radiates and can have an X-ray luminosity of $\sim 10^{42}$ erg/s for galaxies with a gas fraction as low as 10%. Herein lies the difficulty of detecting the shocked gas: the shocked gas is 1000 times less luminous than the non-shocked gas. To observe such X-ray shocks from mergers, one would have to look for a signal 3 orders of magnitude smaller than the global X-ray level *and* the effect only lasts for a timescale that is an order of magnitude shorter than the merger. Merger-induced star formation and AGN activity adds to the confusion by contributing X-rays from accretion disks.

The redeeming feature of our predictions comes from the fact that the X-ray emission occurs even when the galaxy separation is large and occurs in a region where the X-ray background is low. Therefore, the ideal procedure to validate our predictions would be to observe close pairs of galaxies with an undisturbed morphology (indicating that the first pass has not occurred), with current space telescopes like *Chandra* and *XMM-Newton*. In such a case, there will be no contamination from merger-associated starbursts and the L_X signature, if observed, could be uniquely ascribed to shocked halo gas. Our simulations assume that the gas is always heated to the virial temperature in galaxies, irrespective of the galaxy mass; recent numerical simulations predict that that may not be the case (Kereš et al. 2005). Smaller mass galaxies, similar to the smallest galaxy we simulated (with $v_{\text{circ}} = 74$ km/s), are not expected to heat above $10^{4.5}$ K. In such a scenario, the predicted L_X from shocks will be much lower. We can use this prediction to constrain the theories of galaxy formation (both semi-analytic and from numerical simulations) against actual observations.

A detailed analysis of the feasibility of the X-ray detection is beyond the scope of this paper; however, we will assume a conservative threshold of the X-ray flux as 10^{-15} erg/s/cm² and some representative distance to galaxy pairs of ~ 20 Mpc. This sets a detection threshold in the X-ray luminosity of 5×10^{37} erg/s. We will find the hot halo itself exceeds this threshold for all the simulations but the shock X-ray luminosity does not always do so. We empirically model the peak L_X from shocks based on our set of 36 simulations as follows:

$$\log_{10} \left[\frac{L_{\text{peak}}}{10^{38} \text{ erg/s}} \right] = 0.88 \times \log_{10} \Delta H - 1.25. \quad (9)$$

Note that we have modelled L_X completely by thermal bremsstrahlung, which is a fairly inefficient radiation mechanism at $\sim 10^{6.2}$ K. Using *XSPEC*, we find if that gas is at solar metallicity, the total emission will increase by more than an order of magnitude. Thus, our predictions about L_X should be considered a lower limit to the likely X-ray emission in actual observations of colliding galaxies for a given hot gas mass.

Our simulations show that gas escapes from galaxies during the course of the merger, with most of the gas propelled outside $3 R_{\text{vir}}$ even before the final merger event. For equal-mass mergers, the unbound gas fraction ranges from 10-20% depending on the impact parameter and orbit type. The unequal-mass mergers result in 3-5% unbound gas, with similar fractions coming from each of the merging galaxies. All of this unbound gas, presumably enriched with metals, flows out into the IGM. Observations of the IGM at low redshift show the presence of metals (Danforth & Shull 2008); cosmological simulations can account for the metals since it only takes trace amounts of metals to leave a large-scale signature. However, about 50% of the baryons are actually present in the IGM (Fukugita & Peebles 2004) in a temperature-density phase-space that is difficult to probe via observations (Danforth & Shull 2008). For about a decade, numerical simulations of structure formation have been struggling to obtain a prescription that allows such large amounts of gas to escape from galaxies without violating other observational constraints like the star formation rate. Our results show that mergers are an effective way to extract gravitational energy and cause significant mass-loss from galaxies. This process is similar, in principle, to the gravitational heating that has been incorporated for the first time in semi-analytic galaxy formation recipes in a recent paper (Khochfar & Ostriker 2008). Our simulations provide the empirical fits that can be incorporated into such semi-analytic simulations. Though the amount of gas has a strong dependence on the initial orbital energies, we see that each merger releases $\gtrsim 2 \times 10^{10} M_{\odot}$ of material into the IGM. Given that each galaxy suffers a major merger in its past (Conselice et al. 2003), the total amount of unbound gas can become significant over the lifetime of the Universe. We calculate this in a companion paper (Sinha & Holley-Bockelmann 2009).

We use those merger remnants with unbound fractions larger than 3% to obtain a prescription for the unbound gas fraction as a function of the merger impulse, ΔE , as follows:

$$f_{\text{unb}} = 3.14 \times \log_{10} \Delta E - 0.16. \quad (10)$$

Overall, both X-ray shocks and the unbound gas production are two facets of the same phenomena: the conversion of gravitational potential energy into thermal and kinetic energy. Even though cooling, star formation and other baryonic physics

were not included in our simulations, the tremendous amount of available gravitational potential energy and the subsequent conversion of a fraction of it into thermal energy continuously heats the gas at a much faster rate than it can cool via any feasible cooling mechanism, at least for the temperatures and densities involved in our simulations.

Cox et al. (2004) showed that it is possible to repopulate the halo with gas (and metals) via mergers of disk galaxies; mass-loaded stellar winds from high mass stars, and AGN activity can also enrich the gas in the halo. We know that the metal content of the gas can strongly enhance the X-ray production, even overshadowing the contribution from thermal bremsstrahlung. For example, for solar metallicity gas at 10^6 K, the emission for a MEKAL model is 2 orders of magnitude larger than that of thermal bremsstrahlung. As part of a future project, we will include metals in the merging galaxies to determine how this affects the X-ray properties. We expect that the boost from metal line emission will make the emission more detectable, and may allow X-ray shocks to be observed for galaxy pairs with larger separations.

Our simulations were performed with vacuum boundary conditions, but in reality galaxies are continuously evolving objects within the background of an expanding Universe. Pristine gas is falling into the haloes, and the haloes themselves are growing more massive. Cosmological simulations are required to fully model the mergers within the context of an evolving background. As part of a future project, we will use cosmological simulations with dark matter and gas to explore the phenomena of the shocks in the mergers.

An important implication of this work is that using our fitting formulae we can estimate the total emission in X-rays from shocks and the total amount of unbound gas as a function of z over the history of the Universe. To do this, we will combine an extended Press-Schechter formalism (Lacey & Cole 1993; Bower 1991; Bond et al. 1991) with our empirical fits, in a semi-analytic approach. The semi-analytic estimate for the unbound gas fraction over the lifetime of the Universe can be compared against the current gas fractions of galaxies as well as the baryonic content of the IGM. We will explore the evolution of the unbound gas fraction of the Universe in Sinha & Holley-Bockelmann (2009).

REFERENCES

- Allen, S. W., Schmidt, R. W., & Fabian, A. C. 2002, *MNRAS*, 334, L11
- Barnes, J. & Hut, P. 1986, *Nature*, 324, 446
- Barnes, J. E. 2002, *MNRAS*, 333, 481
- Barnes, J. E. & Hernquist, L. 1992, *ARA&A*, 30, 705
- . 1996, *ApJ*, 471, 115
- Barnes, J. E. & Hernquist, L. E. 1991, *ApJ*, 370, L65
- Benson, A. J. 2005, *MNRAS*, 358, 551
- Bhattacharya, S., di Matteo, T., & Kosowsky, A. 2008, *MNRAS*, 389, 34
- Bond, J. R., Cole, S., Efstathiou, G., & Kaiser, N. 1991, *ApJ*, 379, 440
- Borgani, S., Governato, F., Wadsley, J., Menci, N., Tozzi, P., Quinn, T., Stadel, J., & Lake, G. 2002, *MNRAS*, 336, 409
- Bower, R. G. 1991, *MNRAS*, 248, 332
- Bregman, J. N. 2007, *ARA&A*, 45, 221
- Bullock, J. S., Kolatt, T. S., Sigad, Y., Somerville, R. S., Kravtsov, A. V., Klypin, A. A., Primack, J. R., & Dekel, A. 2001, *MNRAS*, 321, 559
- Casasola, V., Bettoni, D., & Galletta, G. 2004, *A&A*, 422, 941
- Cavaliere, A. & Fusco-Femiano, R. 1976, *A&A*, 49, 137
- Cen, R. & Ostriker, J. P. 1999, *ApJ*, 519, L109
- . 2006, *ApJ*, 650, 560
- Combes, F., Prugniel, P., Rampazzo, R., & Sulentic, J. W. 1994, *A&A*, 281, 725
- Conselice, C. J., Bershady, M. A., Dickinson, M., & Papovich, C. 2003, *AJ*, 126, 1183
- Covington, M., Dekel, A., Cox, T. J., Jonsson, P., & Primack, J. R. 2008, *MNRAS*, 384, 94
- Cowie, L. L., Songaila, A., Kim, T.-S., & Hu, E. M. 1995, *AJ*, 109, 1522
- Cox, T. J., Di Matteo, T., Hernquist, L., Hopkins, P. F., Robertson, B., & Springel, V. 2006, *ApJ*, 643, 692
- Cox, T. J., Primack, J., Jonsson, P., & Somerville, R. S. 2004, *ApJ*, 607, L87
- Croton, D. J., Springel, V., White, S. D. M., De Lucia, G., Frenk, C. S., Gao, L., Jenkins Kauffmann, G., Navarro, J. F., & Yoshida, N. 2006, *MNRAS*, 365, 11
- Danforth, C. W. & Shull, J. M. 2008, *ApJ*, 679, 194
- Davé, R., Hernquist, L., Katz, N., & Weinberg, D. H. 1999, *ApJ*, 511, 521
- Davé, R. & Oppenheimer, B. D. 2007, *MNRAS*, 374, 427
- Di Matteo, T., Colberg, J., Springel, V., Hernquist, L., & Sijacki, D. 2008, *ApJ*, 676, 33
- Di Matteo, T., Springel, V., & Hernquist, L. 2005, *Nature*, 433, 604
- Dubinski, J., Mihos, J. C., & Hernquist, L. 1999, *ApJ*, 526, 607
- Eke, V. R., Cole, S., Frenk, C. S., & Patrick Henry, J. 1998, *MNRAS*, 298, 1145
- Fakhouri, O. & Ma, C.-P. 2008, *MNRAS*, 386, 577
- Ferrara, A., Pettini, M., & Shchekinov, Y. 2000, *MNRAS*, 319, 539
- Fransson, C. & Epstein, R. 1982, *MNRAS*, 198, 1127
- Fukugita, M., Hogan, C. J., & Peebles, P. J. E. 1998, *ApJ*, 503, 518
- Fukugita, M. & Peebles, P. J. E. 2004, *ApJ*, 616, 643
- Gingold, R. A. & Monaghan, J. J. 1977, *MNRAS*, 181, 375
- Governato, F., Willman, B., Mayer, L., Brooks, A., Stinson, G., Valenzuela, O., Wadsley, J., & Quinn, T. 2007, *MNRAS*, 374, 1479
- Hernquist, L. & Mihos, J. C. 1995, *ApJ*, 448, 41
- Holmberg, E. 1941, *ApJ*, 94, 385
- Hopkins, P. F., Hernquist, L., Cox, T. J., Di Matteo, T., Robertson, B., & Springel, V. 2006, *ApJS*, 163, 1
- Jones, C. & Forman, W. 1984, *ApJ*, 276, 38
- Kannappan, S. J. 2004, *ApJ*, 611, L89
- Kereš, D., Katz, N., Weinberg, D. H., & Davé, R. 2005, *MNRAS*, 363, 2
- Khochfar, S. & Burkert, A. 2006, *A&A*, 445, 403
- Khochfar, S. & Ostriker, J. P. 2008, *ApJ*, 680, 54
- Kobayashi, C., Springel, V., & White, S. D. M. 2007, *MNRAS*, 376, 1465
- Lacey, C. & Cole, S. 1993, *MNRAS*, 262, 627
- Laine, S., van der Marel, R. P., Rossa, J., Hibbard, J. E., Mihos, J. C., Böker, T., & Zabludoff, A. I. 2003, *AJ*, 126, 2717
- Leccardi, A. & Molendi, S. 2008, *A&A*, 486, 359
- Lokas, E. L. & Mamon, G. A. 2001, *MNRAS*, 321, 155
- Mac Low, M.-M. & Ferrara, A. 1999, *ApJ*, 513, 142

- Mathews, W. G. & Brighenti, F. 2003, *ARA&A*, 41, 191
- Mathur, S., Weinberg, D. H., & Chen, X. 2003, *ApJ*, 582, 82
- Mihos, J. C. & Hernquist, L. 1994, *ApJ*, 431, L9
- . 1996, *ApJ*, 464, 641
- Murali, C. 2000, *ApJ*, 529, L81
- Navarro, J. F., Frenk, C. S., & White, S. D. M. 1997, *ApJ*, 490, 493
- Nicastro, F., Mathur, S., Elvis, M., Drake, J., Fiore, F., Fang, T., Fruscione, A., Krongold, Y., Marshall, H., & Williams, R. 2005, *ApJ*, 629, 700
- Oppenheimer, B. D. & Davé, R. 2008, *MNRAS*, 387, 577
- O’Sullivan, E., Forbes, D. A., & Ponman, T. J. 2001, *MNRAS*, 328, 461
- Pedersen, K., Rasmussen, J., Sommer-Larsen, J., Toft, S., Benson, A. J., & Bower, R. G. 2006, *New Astronomy*, 11, 465
- Penton, S. V., Stocke, J. T., & Shull, J. M. 2004, *ApJS*, 152, 29
- Power, C., Navarro, J. F., Jenkins, A., Frenk, C. S., White, S. D. M., Springel, V., Stadel, J., & Quinn, T. 2003, *MNRAS*, 338, 14
- Roberts, T. P., Warwick, R. S., Ward, M. J., & Murray, S. S. 2002, *MNRAS*, 337, 677
- Sanders, D. B. & Mirabel, I. F. 1996, *ARA&A*, 34, 749
- Scannapieco, C., Tissera, P. B., White, S. D. M., & Springel, V. 2006, *MNRAS*, 371, 1125
- . 2008, *MNRAS*, 389, 1137
- Scannapieco, E., Silk, J., & Bouwens, R. 2005, *ApJ*, 635, L13
- Schweizer, F. 1986, *Science*, 231, 227
- Sembach, K. R., Wakker, B. P., Savage, B. D., Richter, P., Meade, M., Shull, J. M., Jenkins, E. B., Sonneborn, G., & Moos, H. W. 2003, *ApJS*, 146, 165
- Sijacki, D., Springel, V., di Matteo, T., & Hernquist, L. 2007, *MNRAS*, 380, 877
- Sinha, M. & Holley-Bockelmann, K. 2009, in prep.
- Snowden, S. L., Egger, R., Freyberg, M. J., McCammon, D., Plucinsky, P. P., Sanders, W. T., Schmitt, J. H. M. M., Truemper, J., & Voges, W. 1997, *ApJ*, 485, 125
- Springel, V. 2005, *MNRAS*, 364, 1105
- Springel, V., Di Matteo, T., & Hernquist, L. 2005, *ApJ*, 620, L79
- Springel, V. & Hernquist, L. 2002, *MNRAS*, 333, 649
- . 2003, *MNRAS*, 339, 312
- Springel, V. & White, S. D. M. 1999, *MNRAS*, 307, 162
- Springel, V., Yoshida, N., & White, S. D. M. 2001, *New Astronomy*, 6, 79
- Thacker, R. J. & Couchman, H. M. P. 2000, *ApJ*, 545, 728
- Thacker, R. J., Scannapieco, E., & Couchman, H. M. P. 2006, *ApJ*, 653, 86
- Toomre, A. & Toomre, J. 1972, *ApJ*, 178, 623
- Vikhlinin, A., Markevitch, M., Murray, S. S., Jones, C., Forman, W., & Van Speybroeck, L. 2005, *ApJ*, 628, 655
- Wang, B. 1995, *ApJ*, 444, L17
- White, S. D. M. & Frenk, C. S. 1991, *ApJ*, 379, 52
- White, S. D. M. & Rees, M. J. 1978, *MNRAS*, 183, 341
- Zwaan, M. A., Staveley-Smith, L., Koribalski, B. S., Henning, P. A., Kilborn, V. A., Ryder, S. D., Barnes, D. G., Bathal, R., Boyce, P. J., de Blok, W. J. G., Disney, M. J., Drinkwater, M. J., Ekers, R. D., Freeman, K. C., Gibson, B. K., Green, A. J., Haynes, R. F., Jerjen, H., Juraszek, S., Kesteven, M. J., Knezek, P. M., Kraan-Korteweg, R. C., Mader, S., Marquarding, M., Meyer, M., Minchin, R. F., Mould, J. R., O’Brien, J., Oosterloo, T., Price, R. M., Putman, M. E., Ryan-Weber, E., Sadler, E. M., Schröder, A., Stewart, I. M., Stootman, F., Warren, B., Waugh, M., Webster, R. L., & Wright, A. E. 2003, *AJ*, 125, 2842